

An immersed peridynamics model of fluid-structure interaction accounting for material damage and failure

Keon Ho Kim¹, Amneet P. S. Bhalla², and Boyce E. Griffith^{3,4,5,6}

¹Department of Mathematics, University of North Carolina, Chapel Hill, NC, USA

²Department of Mechanical Engineering, San Diego State University, San Diego, CA, USA

³Departments of Mathematics, Applied Physical Sciences, and Biomedical Engineering,
University of North Carolina, Chapel Hill, NC, USA

⁴Carolina Center for Interdisciplinary Applied Mathematics, University of North Carolina,
Chapel Hill, NC, USA

⁵Computational Medicine Program, University of North Carolina, Chapel Hill, NC, USA

⁶McAllister Heart Institute, University of North Carolina, Chapel Hill, NC, USA
keonho@email.unc.edu, asbhalla@sdsu.edu, and boyceg@email.unc.edu

July 31, 2022

Abstract

This paper develops and benchmarks an immersed peridynamics method to simulate the deformation, damage, and failure of hyperelastic materials within a fluid-structure interaction framework. The immersed peridynamics method describes an incompressible structure immersed in a viscous incompressible fluid. It expresses the momentum equation and incompressibility constraint in Eulerian form, and it describes the structural motion and resultant forces in Lagrangian form. Coupling between Eulerian and Lagrangian variables is achieved by integral transforms with Dirac delta function kernels, as in standard immersed boundary (IB) methods. The major difference between our approach and conventional IB methods is that we use peridynamics, instead of classical continuum mechanics, to determine the structural forces. We focus on non-ordinary state-based peridynamic material descriptions that allow us to use a constitutive correspondence framework that can leverage well characterized nonlinear constitutive models of soft materials. The convergence and accuracy of our approach are compared to both conventional and immersed finite element methods using widely used benchmark problems of nonlinear incompressible elasticity. We demonstrate that the immersed peridynamics method yields comparable accuracy with similar numbers of structural degrees of freedom for several choices of the size of the peridynamic horizon. We also demonstrate that the method can generate grid-converged simulations of fluid-driven material damage growth, crack formation and propagation, and rupture under large deformations.

Keywords: Immersed peridynamics method, fluid-structure interaction, material damage and failure, non-ordinary state-based peridynamics, constitutive correspondence, incompressible hyperelasticity

1 Introduction

Under extreme loading conditions, structural deformations can cause material damage and, ultimately, failure. Conventional continuum mechanics models are formulated in terms of *local* definitions of strain, which are evaluated using the derivatives of the deformation field, but such derivatives become ill-defined along propagating crack surfaces, where the deformation field becomes *discontinuous*. These discontinuities make it challenging to simulate structural mechanics in the face of material failure using conventional continuum approaches, particularly if the failure event involves an evolving crack front that is not known in advance but instead must be determined by the model. Nonetheless, continuum approaches to describing material failure

have been developed, including linear elastic fracture mechanics (LEFM) [1] using the finite element (FE) method, and substantial work has created numerical methods for simulating fracture, such as the cohesive zone model (CZM) [2] and the eXtended finite element method (XFEM) [3], although these formulations can present challenges themselves in terms of implementation and efficient computation.

As an alternative to local approaches to fracture mechanics, Silling introduced a *non-local* formulation of solid mechanics called *peridynamics* [4], which avoids the use of derivatives in determining strains and instead considers interactions among all material points within a finite *horizon*. Such non-local models can be better suited for simulating material failure than conventional continuum mechanics formulations because they can tolerate discontinuous deformation fields. Silling’s first theory of peridynamics is now known as *bond-based peridynamics* (BB-PD). BB-PD asserts that the forces acting between two interacting particles in a material body are completely determined by the relative positions of the particles in the reference and current configurations (i.e., the reference and deformed *bonds*). This formulation further requires that the resulting *bond forces* are parallel to the deformed bonds in the current configuration. The assumptions of BB-PD impose strong restrictions on the types of materials that can be modeled. Specifically, the BB-PD theory can only describe isotropic materials with a Poisson ratio of $\nu = \frac{1}{3}$ for plane stress and $\nu = \frac{1}{4}$ for plane strain [5].

Silling et al. [6] subsequently introduced *state-based peridynamics*, which overcomes many of the limitations of bond-based formulations. State-based peridynamics adopts the concept of *peridynamic states*. Examples of peridynamic states include the force vector state and the deformation vector state, which are detailed in Sec. 2.1. Whereas a constitutive model in a standard continuum mechanics formulation relates the (local) stress and the (local) strain, a constitutive model in the state-based peridynamic theory is a relationship between the force vector state and the deformation vector state. In ordinary state-based peridynamics (OSB-PD), the force vectors between any two particles may differ in magnitude but are always parallel to the deformed bond. In contrast, the force vectors in non-ordinary state-based peridynamics (NOSB-PD) can differ both in magnitude and direction, which is far more general than BB-PD or OSB-PD and is helpful for developing peridynamic models for real materials. In addition, the force vectors can be determined using non-local analogues of the stress and strain tensors in classical continuum mechanics, which allows these methods to generate non-local generalizations of existing continuum material models.

This paper uses NOSB-PD [6, 7] to simulate the deformations of soft materials under fluid-structure interaction (FSI). To treat FSI, we use the framework of the immersed boundary (IB) method [8]. The IB method for FSI was introduced by Peskin in 1972 to simulate the dynamics of heart valves [9, 10], and it has been used in a broad range of applications, including cardiovascular dynamics [11–21], esophageal transport [22, 23], aquatic locomotion [24–29], and insect flight [30, 31]. The IB method uses Lagrangian variables for the deformations, stresses, and resultant forces of the immersed structure and Eulerian variables for the momentum, viscosity, and incompressibility of the coupled fluid-structure system. Coupling between Lagrangian and Eulerian variables is mediated by integral transforms with Dirac delta function kernels in the continuous formulation. In discretized IB formulations, the singular delta function is replaced by a regularized delta function [8]. This coupling approach enables nonconforming discretizations of the fluid and immersed structures [32, 33].

Conventional IB methods use the framework of nonlinear continuum mechanics to compute the elastic body forces of the immersed structure [33–36]. In this work, the constitutive correspondence model of NOSB-PD is used to compute structural forces instead of continuum mechanics. This approach enables simulations including nonlinear hyperelastic material responses, even with discontinuities in the displacement field (i.e., material damage and failure), which is challenging with continuum-based IB methods. A variety of solid mechanics benchmarks in both two and three spatial dimensions is used to demonstrate the accuracy and efficiency of the resulting immersed peridynamics (IPD) method, including the compressed block [37], Cook’s membrane [38], and the torsion test [39]. All benchmarks show that the accuracy of the structural deformations obtained by the proposed method is comparable to that yielded by a stabilized finite element method [37] and a stabilized immersed finite element-finite difference method [40] for incompressible nonlinear elasticity. Material responses under fluid traction boundary conditions are investigated using both static and dynamic versions of an elastic band test [40]. A modified elastic band with and without an initial crack is used to simulate purely fluid-driven material failure. Some test cases involve interactions between flexible and rigid structures. We treat rigidity constraints by an approximate Lagrange multiplier approach like those developed by Glowinski and co-workers [41–43].

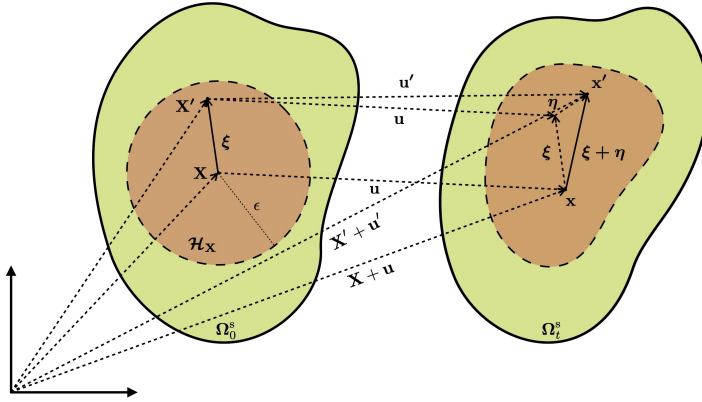


Figure 1: Peridynamic material points, bonds, and horizons in the reference and current configurations.

2 Non-ordinary state-based peridynamics

This section presents a non-ordinary state-based peridynamic (NOSB-PD) formulation [6, 7] that can be used with material models that are characterized by strain energy functionals, such as those often used with continuum mechanics (CM) descriptions of hyperelastic materials. We first describe the continuous formulation of the peridynamic model and next introduce the simple spatial discretization that we use in computational tests of our immersed peridynamics (IPD) method for fluid-structure interaction.

2.1 Peridynamic states

The dynamics of an elastic body occupying the region Ω_t^s at time t are described using material (reference) coordinates $\mathbf{X} \in \Omega_0^s$, and the deformation mapping $\chi : (\Omega_0^s, t) \mapsto \Omega_t^s$ is used to relate the reference and deformed coordinate systems, so that $\mathbf{x} = \chi(\mathbf{X}, t)$ is the physical position of the material point \mathbf{X} at time t . Each material point \mathbf{X} in peridynamics interacts with all material points within a finite region around \mathbf{X} called the *horizon* and denoted as $\mathcal{H}_{\mathbf{X}}$. Here, $\mathcal{H}_{\mathbf{X}}$ is assumed as the sphere of radius ϵ centered at \mathbf{X} , but other choices of the horizon shape have also been used in practice (e.g., a cube of side length 2ϵ)¹. A material point \mathbf{X} interacts with each point \mathbf{X}' in its horizon $\mathcal{H}_{\mathbf{X}}$ through a *bond*, which is defined in the reference frame by $\boldsymbol{\xi} = \mathbf{X}' - \mathbf{X}$, and which deforms to $\boldsymbol{\xi} + \boldsymbol{\eta} = \mathbf{x}' - \mathbf{x}$ in the deformed frame, with $\mathbf{x}' = \chi(\mathbf{X}', t)$ and $\mathbf{x} = \chi(\mathbf{X}, t)$. See Fig. 1. \mathbf{u} and \mathbf{u}' represent the displacements of the material points labeled by \mathbf{X} and \mathbf{X}' from the reference configuration to the deformed configuration, respectively, so that $\mathbf{x} = \mathbf{X} + \mathbf{u}$ and $\mathbf{x}' = \mathbf{X}' + \mathbf{u}'$. The deformed bond is $\mathbf{x}' - \mathbf{x} = (\mathbf{X}' + \mathbf{u}') - (\mathbf{X} + \mathbf{u}) = (\mathbf{X}' - \mathbf{X}) + (\mathbf{u}' - \mathbf{u}) = \boldsymbol{\xi} + \boldsymbol{\eta}$. The definition of *deformation vector state* \mathbf{Y} is motivated by this consideration:

$$\mathbf{Y} = \mathbf{Y}[\mathbf{X}, t](\boldsymbol{\xi}) = \chi(\mathbf{X} + \boldsymbol{\xi}, t) - \chi(\mathbf{X}, t) = \mathbf{x}' - \mathbf{x}. \quad (1)$$

Thus, $\mathbf{Y}[\mathbf{X}, t](\boldsymbol{\xi})$ is the deformation of the bond $\boldsymbol{\xi}$ associated with material point \mathbf{X} at time t .

The *force vector state* associated with a bond $\boldsymbol{\xi}$ associated with material point \mathbf{X} at time t is denoted by

$$\mathbf{T} = \mathbf{T}[\mathbf{X}, t](\boldsymbol{\xi}). \quad (2)$$

Constitutive models in state-based peridynamics provide the values for the force vector state field based on the deformation state and possibly other variables:

$$\mathbf{T} = \hat{\mathbf{T}}(\mathbf{Y}, \Lambda), \quad (3)$$

in which Λ denotes all variables that determine the force state other than the deformation state. There are several restrictions on the force vectors based on different material models. For example, the force vector

¹In the peridynamics literature, the horizon size is commonly denoted by δ , but here we reserve that symbol for the Dirac delta function.

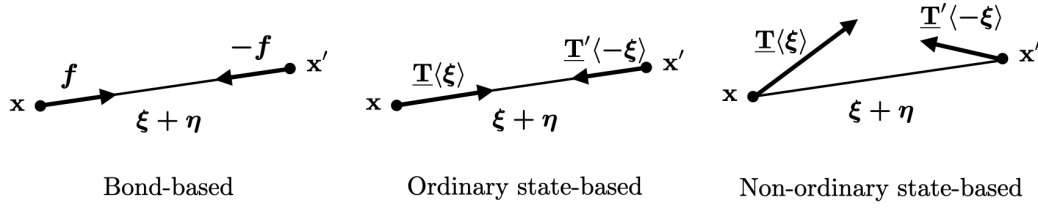


Figure 2: Force vector states for bond-based, ordinary state-based, and non-ordinary state-based peridynamics.

state of an *ordinary* material is defined by

$$\underline{\mathbf{T}} = \underline{t} \underline{\mathbf{M}}, \quad (4)$$

in which $\underline{\mathbf{M}}$ is the deformed direction vector state that is the unit directional vector of the deformed vector state $\underline{\mathbf{Y}}$ and \underline{t} is the scalar force state. In ordinary peridynamic material models, the force vectors are parallel to its deformed bond. If the force vectors are not parallel to its corresponding bond in the deformed configuration, the material description is called non-ordinary. Here, we primarily focus on NOSB-PD for nonlinear material responses because it allows us to leverage existing hyperelastic constitutive laws for soft materials. Fig. 2 illustrates possible force vector states for bond-based, ordinary state-based, and non-ordinary state-based peridynamics. Silling et al. [6] provide additional details about peridynamic states.

2.2 Kinematics and balance laws

In a state-based peridynamic model, the basic equation of motion is

$$\rho_0 \frac{\partial^2 \mathbf{u}}{\partial t^2}(\mathbf{X}, t) = \int_{\mathcal{H}_{\mathbf{x}}} (\underline{\mathbf{T}}[\mathbf{X}, t]\langle\xi\rangle - \underline{\mathbf{T}}[\mathbf{X}', t]\langle-\xi\rangle) d\mathbf{X}' + \mathbf{b}(\mathbf{X}, t), \quad (5)$$

in which ρ_0 is the mass density of the material and $\mathbf{b}(\mathbf{X}, t)$ is an external force density. The pairwise bond force function $\mathbf{F}_{\text{PD}}(\mathbf{X}', \mathbf{X}, t)$ is

$$\mathbf{F}_{\text{PD}}(\mathbf{X}', \mathbf{X}, t) = \underline{\mathbf{T}}[\mathbf{X}, t]\langle\xi\rangle - \underline{\mathbf{T}}[\mathbf{X}', t]\langle-\xi\rangle, \quad (6)$$

which accounts for contributions of the material model at both \mathbf{X} and \mathbf{X}' to balance linear momentum. Note that force balance is automatically satisfied for arbitrary force vector states:

$$\mathbf{F}_{\text{PD}}(\mathbf{X}, \mathbf{X}', t) = \underline{\mathbf{T}}[\mathbf{X}, t]\langle\xi\rangle - \underline{\mathbf{T}}[\mathbf{X}', t]\langle-\xi\rangle = -(\underline{\mathbf{T}}[\mathbf{X}', t]\langle-\xi\rangle - \underline{\mathbf{T}}[\mathbf{X}, t]\langle\xi\rangle) = -\mathbf{F}_{\text{PD}}(\mathbf{X}', \mathbf{X}, t), \quad (7)$$

which is consistent with Newton's third law of motion. Conservation of linear momentum is guaranteed in all three peridynamic models for any definition of the force vector states:

$$\int_{\Omega_0^s} \int_{\mathcal{H}_{\mathbf{x}}} (\underline{\mathbf{T}}[\mathbf{X}, t]\langle\xi\rangle - \underline{\mathbf{T}}[\mathbf{X}', t]\langle-\xi\rangle) d\mathbf{X}' d\mathbf{X}, \quad (8)$$

$$= \int_{\Omega_0^s} \int_{\Omega_0^s} (\underline{\mathbf{T}}[\mathbf{X}, t]\langle\xi\rangle - \underline{\mathbf{T}}[\mathbf{X}', t]\langle-\xi\rangle) d\mathbf{X}' d\mathbf{X}, \quad (9)$$

$$= \int_{\Omega_0^s} \int_{\Omega_0^s} \underline{\mathbf{T}}[\mathbf{X}, t]\langle\xi\rangle d\mathbf{X}' d\mathbf{X} - \int_{\Omega_0^s} \int_{\Omega_0^s} \underline{\mathbf{T}}[\mathbf{X}', t]\langle-\xi\rangle d\mathbf{X}' d\mathbf{X}, \quad (10)$$

$$= \int_{\Omega_0^s} \int_{\Omega_0^s} \underline{\mathbf{T}}[\mathbf{X}, t]\langle\xi\rangle d\mathbf{X}' d\mathbf{X} - \int_{\Omega_0^s} \int_{\Omega_0^s} \underline{\mathbf{T}}[\mathbf{X}, t]\langle\xi\rangle d\mathbf{X} d\mathbf{X}', \quad (11)$$

$$= \int_{\Omega_0^s} \int_{\Omega_0^s} \underline{\mathbf{T}}[\mathbf{X}, t]\langle\xi\rangle d\mathbf{X}' d\mathbf{X} - \int_{\Omega_0^s} \int_{\Omega_0^s} \underline{\mathbf{T}}[\mathbf{X}, t]\langle\xi\rangle d\mathbf{X}' d\mathbf{X}, \quad (12)$$

$$= \mathbf{0}. \quad (13)$$

Note that $\underline{\mathbf{T}}[\mathbf{X}, t]\langle \boldsymbol{\xi} \rangle = \underline{\mathbf{T}}[\mathbf{X}', t]\langle -\boldsymbol{\xi} \rangle = \mathbf{0}$ for all $\mathbf{X}' \notin \mathcal{H}_{\mathbf{X}}$, so that the integration domain can be taken as the entire solid domain Ω_0^s .

Balance of angular momentum holds if

$$\int_{\mathcal{H}_{\mathbf{X}}} (\underline{\mathbf{Y}}[\mathbf{X}, t]\langle \boldsymbol{\xi} \rangle \times \underline{\mathbf{T}}[\mathbf{X}, t]\langle \boldsymbol{\xi} \rangle) d\mathbf{X}' = \mathbf{0}. \quad (14)$$

Eq. (14) is automatically satisfied if the force vector $\underline{\mathbf{T}}$ is aligned with its corresponding deformed bond $\underline{\mathbf{Y}}$; however, the force vector in NOSB-PD is not parallel to its relative position vector in general, so there is a need to define the force vector state in a way that satisfies the conservation of angular momentum.

2.3 Constitutive correspondence

In classical continuum mechanics, the *local deformation gradient tensor* is

$$\mathbb{F}_{\text{local}} = \frac{\partial \boldsymbol{\chi}}{\partial \mathbf{X}}, \quad (15)$$

which determines the local spatial deformation of a point. The local stress and strain tensors are computed using the local deformation gradient tensor with various choices of constitutive models. For a hyperelastic material model, the first Piola-Kirchhoff stress tensor is determined from a strain energy functional Ψ by

$$\mathbb{P} = \frac{\partial \Psi(\mathbb{F}_{\text{local}})}{\partial \mathbb{F}_{\text{local}}}. \quad (16)$$

Developing a peridynamic model that corresponds to classical nonlinear hyperelasticity in cases that do not involve material failure requires constructing non-local analogues of the deformation gradient tensor and stress. The *non-local deformation gradient tensor* is

$$\mathbb{F}_{\text{non-local}} = \left[\int_{\mathcal{H}_{\mathbf{X}}} \omega(|\boldsymbol{\xi}|) (\underline{\mathbf{Y}}(\boldsymbol{\xi}) \otimes \boldsymbol{\xi}) d\mathbf{X}' \right] \mathbb{K}^{-1}, \quad (17)$$

in which $\omega(|\boldsymbol{\xi}|)$ is a non-negative scalar valued function called the *influence function*, which controls the influence of peridynamic points away from the current point, and \mathbb{K} is the *shape tensor*

$$\mathbb{K} = \int_{\mathcal{H}_{\mathbf{X}}} \omega(|\boldsymbol{\xi}|) (\boldsymbol{\xi} \otimes \boldsymbol{\xi}) d\mathbf{X}'. \quad (18)$$

If the deformation mapping $\boldsymbol{\chi}$ is continuously differentiable and $\mathcal{H}_{\mathbf{X}} \subset \Omega_0^s$, then, by a Taylor expansion, Eq. (17) can be written as

$$\mathbb{F}_{\text{non-local}} = \left[\int_{\mathcal{H}_{\mathbf{X}}} \omega(|\boldsymbol{\xi}|) ((\boldsymbol{\chi}(\mathbf{X} + \boldsymbol{\xi}, t) - \boldsymbol{\chi}(\mathbf{X}, t)) \otimes \boldsymbol{\xi}) d\mathbf{X}' \right] \mathbb{K}^{-1}, \quad (19)$$

$$= \left[\int_{\mathcal{H}_{\mathbf{X}}} \omega(|\boldsymbol{\xi}|) \left(\left(\frac{\partial \boldsymbol{\chi}}{\partial \mathbf{X}} \boldsymbol{\xi} + O(|\boldsymbol{\xi}|^2) \right) \otimes \boldsymbol{\xi} \right) d\mathbf{X}' \right] \mathbb{K}^{-1}, \quad (20)$$

$$= \left[\int_{\mathcal{H}_{\mathbf{X}}} \omega(|\boldsymbol{\xi}|) (\boldsymbol{\xi} \otimes \boldsymbol{\xi}) d\mathbf{X}' \right] \mathbb{K}^{-1} \frac{\partial \boldsymbol{\chi}}{\partial \mathbf{X}} + O(\epsilon^2), \quad (21)$$

$$= \mathbb{F}_{\text{local}} + O(\epsilon^2). \quad (22)$$

Consequently, the non-local deformation gradient tensor is a second-order accurate approximation to the local deformation gradient tensor used in the conventional continuum theory. Near the boundary of the domain where the influence function is not symmetric, however, it is only first-order accurate [44]. Notice that the non-local deformation gradient tensor is not defined only on a particular bond. Rather, it provides an averaged description of all interacting bonds in the horizon of a material point. The integral operators in the peridynamic theory allow for descriptions of discontinuities in materials, such as cracks and fractures. To simplify notation for the remainder of the paper, we denote the non-local deformation gradient tensor in NOSB-PD by \mathbb{F} .

In the NOSB-PD constitutive correspondence introduced by Silling et al. [6], the force vector state is defined by

$$\underline{\mathbf{T}}[\mathbf{X}, t](\boldsymbol{\xi}) = \omega(|\boldsymbol{\xi}|)\mathbb{P}\mathbb{K}^{-1}\boldsymbol{\xi}, \quad (23)$$

in which the first Piola-Kirchhoff stress tensor \mathbb{P} is computed using the non-local deformation gradient tensor instead of the local deformation gradient tensor in Eq. (16). Note that Eq. (23) guarantees the balance of angular momentum [6,7,45]. In brief, once the non-local deformation gradient \mathbb{F} is determined, the first Piola-Kirchhoff stress tensor \mathbb{P} can be obtained from a classical constitutive material model, and consequently the peridynamic force vector is determined. This relation between the conventional stress tensor in continuum mechanics and the peridynamic force vector state is the so-called constitutive correspondence.

2.4 Failure and damage

In peridynamics, the formation and propagation of a crack occurs as bonds break between the Lagrangian material points. In this study, a critical stretch criterion is used to determine if a bond breaks. Other failure criteria have also been suggested, including strain-based criteria [46] and energy-based criteria [47]. Bond breakage is modeled as an irreversible process: once a bond breaks, it cannot be reformed. The bond stretch is

$$s = \frac{|\boldsymbol{\xi} + \boldsymbol{\eta}|}{|\boldsymbol{\xi}|}. \quad (24)$$

If the bond stretch exceeds its critical value s_c , there is no longer interaction between the two material points connected by the bond, i.e, the bond breaks. To track the connectivity between two material points that are initially connected by the bond $\boldsymbol{\xi}$ under deformations, we use an indicator function $I(\boldsymbol{\xi}, t)$ [48]:

$$I(\boldsymbol{\xi}, t) = \begin{cases} 1, & s \leq s_c, \\ 0, & s > s_c. \end{cases} \quad (25)$$

We use a modified influence function $\hat{\omega}(|\boldsymbol{\xi}|, t) = \omega(|\boldsymbol{\xi}|)I(\boldsymbol{\xi}, t)$ that takes the value of 0 if the bond $\boldsymbol{\xi}$ breaks. This also implies that the deformation gradient tensor and force vector state, Eqs. (17) and (23), must be modified after a bond breaks in the material horizon. In contrast, the shape tensor \mathbb{K} does not change with bond breakage.

The local damage at a material point \mathbf{X} at time t can be computed by the bond connectivity within the peridynamic horizon $\mathcal{H}_{\mathbf{X}}$ as [48]

$$\varphi(\mathbf{X}, t) = 1 - \frac{\int_{\mathcal{H}_{\mathbf{X}}} I(\boldsymbol{\xi}, t) d\mathbf{X}'}{\int_{\mathcal{H}_{\mathbf{X}}} d\mathbf{X}'}, \quad (26)$$

which is the volume-weighted ratio of the number of eliminated bonds to the number of initial bonds at a material point within the horizon.

3 Immersed peridynamics method

This section presents the continuous and discrete immersed peridynamics (IPD) formulations for simulating fluid-structure interaction (FSI) with and without material damage and failure.

3.1 Continuous formulation

The continuous IPD formulation considers an Eulerian computational domain Ω that consists of a time-dependent fluid subdomain Ω_t^f and solid subdomain Ω_t^s that are indexed time t . We use both fixed spatial coordinates $\mathbf{x} \in \Omega$ and reference coordinates $\mathbf{X} \in \Omega_0^s$, with Ω_0^s indicating the region occupied by the solid

structure at time $t = 0$. The dynamics of the fluid-structure system are described by

$$\rho \frac{D\mathbf{v}}{Dt}(\mathbf{x}, t) = -\nabla p(\mathbf{x}, t) + \mu \nabla^2 \mathbf{v}(\mathbf{x}, t) + \mathbf{f}(\mathbf{x}, t), \quad (27)$$

$$\nabla \cdot \mathbf{v}(\mathbf{x}, t) = 0, \quad (28)$$

$$\mathbf{f}(\mathbf{x}, t) = \int_{\Omega_0^s} \mathbf{F}(\mathbf{X}, t) \delta(\mathbf{x} - \boldsymbol{\chi}(\mathbf{X}, t)) d\mathbf{X}, \quad (29)$$

$$\frac{\partial \boldsymbol{\chi}}{\partial t}(\mathbf{X}, t) = \mathbf{V}(\mathbf{X}, t) = \int_{\Omega} \mathbf{v}(\mathbf{X}, t) \delta(\mathbf{x} - \boldsymbol{\chi}(\mathbf{X}, t)) d\mathbf{x} = \mathbf{v}(\boldsymbol{\chi}(\mathbf{X}, t), t), \quad (30)$$

in which ρ is the mass density, μ is the viscosity, $\mathbf{v}(\mathbf{x}, t)$ is the Eulerian velocity, $\mathbf{V}(\mathbf{X}, t)$ is the velocity of the structure, $p(\mathbf{x}, t)$ is the Eulerian pressure field, $\mathbf{f}(\mathbf{x}, t)$ is the Eulerian structural force density generated by the deformations of the structure, and $\mathbf{F}(\mathbf{X}, t)$ is the Lagrangian structural force density. The operators ∇ , ∇^2 , and $\nabla \cdot$ are with respect to spatial (current) coordinates, and $\frac{D}{Dt} = \frac{\partial}{\partial t} + \mathbf{v} \cdot \nabla$ is the material time derivative in current coordinates. Eqs. (27) and (28) are the incompressible Navier-Stokes equations. The Eulerian and Lagrangian variables are coupled by integral transforms with Dirac delta function kernels in Eqs. (29) and (30). Notice that Eq. (30) implies that the no-slip boundary condition holds along the fluid-solid interface. Eq. (30) also implies that the structure is exactly incompressible, because its motion is determined by $\mathbf{v}(\mathbf{X}, t)$, which satisfies the incompressible constraint, Eq. (29), throughout the entire computational domain Ω .

Some cases in the present study include both rigid and elastic parts. We approximately impose the rigidity constraint of $\frac{\partial \boldsymbol{\chi}}{\partial t}(\mathbf{X}, t) = \mathbf{0}$ by an approximate Lagrangian multiplier force \mathbf{F}_c of the form:

$$\mathbf{F}_c(\mathbf{X}, t) = \kappa (\mathbf{X} - \boldsymbol{\chi}(\mathbf{X}, t)) - \eta \mathbf{V}(\mathbf{X}, t), \quad (31)$$

in which $\kappa \geq 0$ is a stiffness penalty parameter and $\eta \geq 0$ is a damping penalty parameter. Note that as $\kappa \rightarrow \infty$, $\boldsymbol{\chi}(\mathbf{X}, t) \rightarrow \mathbf{X}$, and $\frac{\partial \boldsymbol{\chi}}{\partial t}(\mathbf{X}, t) \rightarrow \mathbf{0}$, and we recover the exactly rigid model. Adding a damping term reduces numerical oscillations that can occur with finite values of κ . This approach corresponds to a fictitious domain approach like those developed by Glowinski et al. [41–43].

3.2 Discrete formulation

The incompressible Navier-Stokes equations are discretized in space using the second-order finite difference scheme on a staggered Cartesian grid [49]. For simplicity, we describe the spatial discretization in two spatial dimensions. The extension to three spatial dimensions is straightforward. The computational domain $\Omega = [0, L]^2$ is discretized by an $N \times N$ Cartesian grid with a uniform grid spacing $h = L/N$ in x - and y -directions. Let (i, j) label the Cartesian grid cell for integer values of i and j and $0 \leq i, j < N$. The Eulerian velocity $\mathbf{v} = (v_1, v_2)$ is approximated at the centers of the edges of the Cartesian grid cells, $\mathbf{x}_{i-\frac{1}{2}, j} = (ih, (j + \frac{1}{2})h)$ and $\mathbf{x}_{i, j-\frac{1}{2}} = ((i + \frac{1}{2})h, jh)$. The components of the discretized elastic body force density $\mathbf{f} = (f_1, f_2)$ are approximated at the same locations as that of velocity. The pressure p is approximated at the centers of the Cartesian grid cells at positions $\mathbf{x}_{i, j} = ((i + \frac{1}{2})h, (j + \frac{1}{2})h)$. The nonlinear advection term $\mathbf{v} \cdot \nabla \mathbf{v}$ is computed using a version of the piecewise parabolic method (PPM) [50].

In the continuous equations, coupling between Eulerian and Lagrangian variables is achieved by integral transforms with Dirac delta function kernels as Eqs. (29)–(30). In the discrete formulation, the singular delta function is replaced by a regularized delta function δ_h , which is formed as a tensor product of one-dimensional kernel functions and defined by

$$\delta_h(\mathbf{x}) = \prod_{i=1}^2 \delta_h(x_i) = \frac{1}{h^2} \phi\left(\frac{x_1}{h}\right) \phi\left(\frac{x_2}{h}\right), \quad (32)$$

in which $\phi(r)$ is a basic one dimensional immersed boundary kernel function [8]. We use the four-point IB kernel function introduced by Peskin [8] unless otherwise mentioned.

The immersed body Ω_t^s is discretized as a collection of Lagrangian points. Then the volume integral

Eq. (29) can be approximated by

$$(f_1)_{i-\frac{1}{2},j} = \sum_l F_{l,1} \delta_h(\mathbf{x}_{i-\frac{1}{2},j} - \mathbf{X}_l) h^2, \quad (33)$$

$$(f_2)_{i,j-\frac{1}{2}} = \sum_l F_{l,2} \delta_h(\mathbf{x}_{i,j-\frac{1}{2}} - \mathbf{X}_l) h^2, \quad (34)$$

in which $\mathbf{F}_l = (F_{l,1}, F_{l,2})$ is the Lagrangian force density at a Lagrangian marker of index l . Note that the Lagrangian force density is computed by NOSB-PD in the proposed method. We use the notation

$$\mathbf{f} = \mathcal{S}[\chi(\cdot, t)] \mathbf{F}, \quad (35)$$

in which $\mathcal{S}[\chi(\cdot, t)]$ is the discrete force-spreading operator. The structural body interacts with the surrounding fluid by spreading the force to the Eulerian grid and moves with the local fluid velocity. Similarly, Lagrangian and Eulerian velocities can be related by

$$V_{l,1}(\mathbf{X}, t) = \sum_{i,j} (v_1)_{i-\frac{1}{2},j} \delta_h(\mathbf{x}_{i-\frac{1}{2},j} - \chi(\mathbf{X}, t)) h^2, \quad (36)$$

$$V_{l,2}(\mathbf{X}, t) = \sum_{i,j} (v_2)_{i,j-\frac{1}{2}} \delta_h(\mathbf{x}_{i,j-\frac{1}{2}} - \chi(\mathbf{X}, t)) h^2, \quad (37)$$

in which $\mathbf{V}_l = (V_{l,1}, V_{l,2})$ is the Lagrangian velocity at a Lagrangian marker \mathbf{X}_l . We use the notation

$$\mathbf{V} = \mathcal{J}[\chi(\cdot, t)] \mathbf{v}, \quad (38)$$

in which \mathcal{J} is the discrete velocity restriction or interpolation operator. In the present formulation, \mathcal{S} and \mathcal{J} are adjoint operators if evaluated in terms of the same structural configurations [33].

Now we focus on computing the Lagrangian force density \mathbf{F} , Eq. (35), in the IPD formulation, which uses the NOSB-PD constitutive correspondence model to obtain the internal elastic body force. Let $\mathcal{H}_{\mathbf{X}_l} \subset \Omega_0^s$ be the set of interacting neighborhoods of radius ϵ centered at the Lagrangian marker $\mathbf{X}_l \in \Omega_0^s$. It is natural that the spatial integrals in the continuous NOSB-PD formulation are discretized as volume weighted sums. Thus, the non-local deformation gradient tensor \mathbb{F} , Eq. (17), and shape tensor \mathbb{K} , Eq. (18), at the material point \mathbf{X}_l are discretized into finite sums as

$$\mathbb{F}_l = \sum_{\mathbf{X}_m \in \mathcal{H}_{\mathbf{X}_l}} \omega(|\mathbf{X}_m - \mathbf{X}_l|) \underline{\mathbf{Y}}(\mathbf{X}_m - \mathbf{X}_l) \otimes (\mathbf{X}_m - \mathbf{X}_l) \mathbb{K}_l^{-1} V_m, \quad (39)$$

$$\mathbb{K}_l = \sum_{\mathbf{X}_m \in \mathcal{H}_{\mathbf{X}_l}} \omega(|\mathbf{X}_m - \mathbf{X}_l|) (\mathbf{X}_m - \mathbf{X}_l) \otimes (\mathbf{X}_m - \mathbf{X}_l) V_m, \quad (40)$$

in which \mathbf{X}_m is a neighborhood of \mathbf{X}_l in the peridynamic horizon $\mathcal{H}_{\mathbf{X}_l}$ and V_m is the volume occupied by material point \mathbf{X}_m . Likewise, the discretized force vector state of material point \mathbf{X}_l is

$$\underline{\mathbf{T}}[\mathbf{X}_l, t](\mathbf{X}_m - \mathbf{X}_l) = \omega(|\mathbf{X}_m - \mathbf{X}_l|) \mathbb{P}_l \mathbb{K}_l^{-1}(\mathbf{X}_m - \mathbf{X}_l), \quad (41)$$

and the pairwise bond force function is

$$\mathbf{F}_{\text{PD}}(\mathbf{X}_l, \mathbf{X}_m, t) = \omega(|\mathbf{X}_m - \mathbf{X}_l|) (\mathbb{P}_l \mathbb{K}_l^{-1} + \mathbb{P}_m \mathbb{K}_m^{-1})(\mathbf{X}_m - \mathbf{X}_l), \quad (42)$$

in which \mathbb{P}_m and \mathbb{K}_m are the discretized first Piola-Kirchhoff stress tensor and shape tensor of particle \mathbf{X}_m , respectively. The discretized first Piola-Kirchhoff stress tensor is computed by the classical constitutive relations, such as Saint-Venant or neo-Hookean material models, but using the discretized non-local deformation gradient tensor here instead of the classical deformation gradient tensor. Consequently, the net internal body force density at material point \mathbf{X}_l is

$$\mathbf{F}(\mathbf{X}_l, t) = \sum_{\mathbf{X}_m \in \mathcal{H}_{\mathbf{X}_l}} \mathbf{F}_{\text{PD}}(\mathbf{X}_l, \mathbf{X}_m, t) V_m. \quad (43)$$

This peridynamic net bond force is used as an elasticity model for the immersed structure at material point \mathbf{X}_l at time t .

Simulating a failure process during the deformation requires the modification of the discretized non-local deformation tensor and peridynamic force vectors based on the connectivity of internal bonds in an immersed structure at each time. Therefore, in our IPD simulations, we replace the influence function in the integral equations, Eqs. (39)–(42), to the modified influence function $\hat{\omega}(|\boldsymbol{\xi}|, t)$ as explained in Sec. 2.4.

3.3 Computational algorithm

We now briefly outline the key steps of the implementation of the IPD method used in the computational examples in Sec. 4. Let \mathbf{v}^n and $\boldsymbol{\chi}^n$ be the fluid velocity and discrete deformation at time $t^n = n\Delta t$, respectively, in which Δt is the time step size. We use a second-order time stepping scheme [33], as follows:

$$\rho \left(\frac{\mathbf{v}^{n+1} - \mathbf{v}^n}{\Delta t} + \mathcal{N}^{(n+\frac{1}{2})} \right) = -\nabla_h p^{n+\frac{1}{2}} + \mu \nabla_h^2 \left(\frac{\mathbf{v}^{n+1} + \mathbf{v}^n}{2} \right) + \mathbf{f}^{n+\frac{1}{2}}, \quad (44)$$

$$\nabla_h \cdot \mathbf{v}^{n+1} = 0, \quad (45)$$

$$\mathbf{f}^{n+\frac{1}{2}} = \mathcal{S} \left[\boldsymbol{\chi}^{n+\frac{1}{2}} \right] \mathbf{F}^{n+\frac{1}{2}}, \quad (46)$$

$$\frac{\boldsymbol{\chi}^{n+\frac{1}{2}} - \boldsymbol{\chi}^n}{\Delta t/2} = \mathcal{J} \left[\boldsymbol{\chi}^n \right] \mathbf{v}^n, \quad (47)$$

$$\frac{\boldsymbol{\chi}^{n+1} - \boldsymbol{\chi}^n}{\Delta t} = \mathcal{J} \left[\boldsymbol{\chi}^{n+\frac{1}{2}} \right] \left(\frac{\mathbf{v}^{n+1} + \mathbf{v}^n}{2} \right), \quad (48)$$

in which $\mathcal{N}^{(n+\frac{1}{2})} = \frac{3}{2} \mathbf{v}^n \cdot \nabla_h \mathbf{v}^n - \frac{1}{2} \mathbf{v}^{n-1} \cdot \nabla_h \mathbf{v}^{n-1}$ is an explicit approximation to the nonlinear advection term in the differential operator in Eq. (27).

Given the initial positions of the Lagrangian markers, the discrete shape tensor is determined by the bond connections between material points in the reference configuration. Then, as the structure moves, the discretized non-local deformation gradient tensor and pairwise bond force function are computed in each time step to account for structural deformations and changes in connectivity (bond breakage). The net bond force is determined by classical constitutive relations with the discrete peridynamic tensors. The discrete Lagrangian force density $\mathbf{F}^{n+\frac{1}{2}}$ is computed at each Lagrangian marker via Eq. (43). The computational algorithm is performed as follows:

Step 1. Given \mathbf{v}^n and $\boldsymbol{\chi}^n$. Update $\boldsymbol{\chi}^{n+\frac{1}{2}}$ using Eq. (47).

Step 2. Update the non-local deformation gradient tensor and force vector state using Eqs. (39)–(42).

Step 2. Evaluate $\mathbf{F}^{n+\frac{1}{2}}$ using Eq. (43).

Step 3. Spread the intermediate Lagrangian force density to the Eulerian grid using Eq. (46).

Step 4. Solve Eqs. (44)–(45).

Step 5. Update $\boldsymbol{\chi}^{n+1}$ using Eq. (48).

4 Benchmarks

We first investigate standard benchmark problems for hyperelastic materials in the conventional solid mechanics literature, with the structure bodies embedded in an incompressible Newtonian fluid for FSI. Numerical tests detailed in Sec. 4.1 exhibit clear constitutive correspondence between the IPD formulation and benchmark FE and FE based IB results. Afterwards, we focus on fluid-driven material failure through several numerical experiments, as detailed in Sec. 4.2.

The IBAMR software [51, 52] is used for all IPD simulations. IBAMR is a distributed-memory parallel implementation of the IB method with support for Cartesian grid adaptive mesh refinement (AMR). We compare the results obtained using our new IPD method against an immersed finite element-finite difference

(IFED) method [40] that is also implemented in IBAMR, and also to a stabilized finite element (FE) method for the comparison tests for incompressible nonlinear elasticity [37].

It is well known that conventional IB-type methods can suffer from poor volume conservation. The exact incompressibility condition in the continuous IB formulation, Eq. (28), can be lost under the spatial discretization, time stepping errors, and the use of regularized delta function kernels. To improve volume conservation, we adopt a modified neo-Hookean model unless otherwise mentioned, which was previously shown to improve the volume conservation of the IFED method by Vadala-Roth et al. [40]. In the modified neo-Hookean model, the strain energy and elastic stress consist of two parts, isochoric and volumetric,

$$\Psi = \frac{G}{2} \left(J^{-2/3} \text{tr}(\mathbb{C}) - 3 \right) + \frac{\kappa_{\text{stab}}}{2} (\ln J)^2, \quad (49)$$

$$\mathbb{P} = G J^{-2/3} \left(\mathbb{F} - \frac{\text{tr}(\mathbb{C})}{3} \mathbb{F}^{-T} \right) + \kappa_{\text{stab}} \ln(J) \mathbb{F}^{-T}, \quad (50)$$

in which G is the shear modulus, J is the determinant of non-local deformation gradient tensor, $J = \det(\mathbb{F})$, $\mathbb{C} = \mathbb{F}^T \mathbb{F}$ is the right Cauchy-Green strain, and κ_{stab} is the numerical bulk modulus. The numerical Poisson's ratio, ν_{stab} , can be used to define the numerical bulk modulus via

$$\kappa_{\text{stab}} = \frac{2G(1 + \nu_{\text{stab}})}{3(1 - 2\nu_{\text{stab}})}. \quad (51)$$

This volumetric term reinforces the discrete incompressibility of the immersed structure. As in prior work that uses an immersed finite element structural description [40], we test several values of the numerical Poisson's ratio in our benchmarking studies.

Unless otherwise noted, the density and viscosity of the fluid are respectively set to $\rho = 1.0 \frac{\text{g}}{\text{cm}^3}$ and $\mu = 0.01 \frac{\text{dyn}\cdot\text{s}}{\text{cm}^2}$, corresponding to water. For simplicity, we use the same density for both the structure and fluid. The computational domain is $\Omega = [0, L]^d$, in which d is the spatial dimension and L is the length of domain. We define the mesh factor ratio $M_{\text{FAC}} = \frac{\Delta X}{\Delta x}$, in which ΔX and Δx are the Lagrangian and Eulerian grid spacings, respectively. The Eulerian grid size is $\Delta x = \frac{L}{N}$, in which N is the number of Cartesian grid cells in one spatial direction. For the computational efficiency, we use $M_{\text{FAC}} = 0.5$ in our IPD simulations, so that the structure discretization is twice as fine as the background Cartesian grid.

In our numerical simulations, both static and dynamic versions of benchmarks are considered. To efficiently obtain numerical solutions at steady states, the maximum amount of load is applied to the immersed structure using the polynomial $q(t) = -2 \left(\frac{t}{T_1} \right)^3 + 3 \left(\frac{t}{T_1} \right)^2$, in which $T_1 = \alpha T_f$ with $\alpha \in (0, 1)$ is a loading time and T_f is a final simulation time. In static benchmarks, the final simulation time T_f is determined when the velocity \mathbf{V} is approximately zero. In addition, viscous damping force is used in the solid region to dampen oscillations and accelerate reaching steady states. Viscous damping is applied to the immersed structure by adding a damping force $-\eta \mathbf{V}$ to the Lagrangian body force \mathbf{F} , as in Eq. (31), in which $\eta > 0$ is the damping coefficient.

The effect of peridynamic horizon is also investigated in the IPD simulations. For the simplicity, a uniform ϵ -ball is used for the peridynamic horizon. The peridynamic horizon size ϵ is always taken to be a constant multiple of the Lagrangian mesh spacing ΔX in the reference configuration. Consequently, our grid refinement studies consider the ϵ -convergence of the IPD formulation². A larger horizon size implies more interactions between Lagrangian points, and it requires more computations compared to a smaller horizon size. Therefore, finding an optimum horizon size is important for optimizing the computational performance of the method. Our simulations examine different peridynamic horizon sizes for the constitutive correspondence: $\epsilon = 1.015\Delta X$, $2.015\Delta X$, $3.015\Delta X$.

The accuracy of numerical solutions is improved by using a volume correction method [55, 56]:

$$V_m^{(l)} = \begin{cases} V_m & \text{if } |\boldsymbol{\xi}| \leq \epsilon - \frac{\Delta X}{2}, \\ \frac{1}{\Delta X} \left[\epsilon - (|\boldsymbol{\xi}| - \frac{\Delta X}{2}) \right] V_m & \text{if } |\boldsymbol{\xi}| \leq \epsilon + \frac{\Delta X}{2}, \\ 0 & \text{otherwise,} \end{cases} \quad (52)$$

²We remark that the notion of convergence that we call ϵ -convergence is more commonly called δ -convergence in the peridynamics literature [53, 54], in which δ defines the horizon size. As mentioned previously, we avoid using δ to describe the horizon size since we use δ to denote the Dirac delta function and δ_h to denote the regularized delta function.

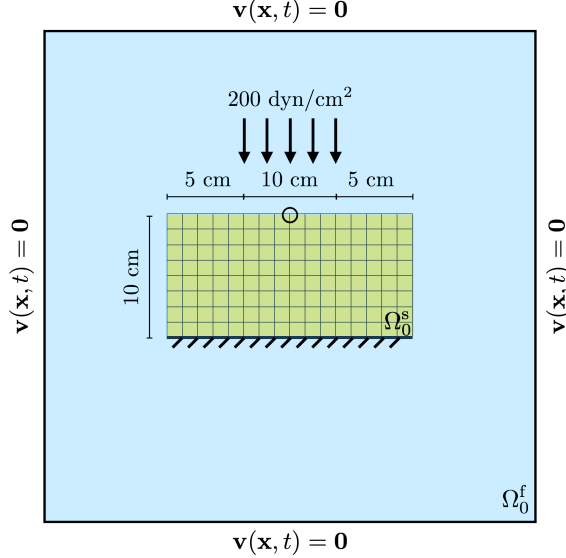


Figure 3: Schematic diagram for the compression test (Sec. 4.1.1). The initial configurations of the immersed structure and a fluid are denoted by Ω_0^s and Ω_0^f , respectively. The entire computational domain is $\Omega = \Omega_0^s \cup \Omega_0^f$. Zero fluid velocity is enforced on the outer boundaries of the computational domain.

in which ξ is a bond connecting material points \mathbf{X}_l and \mathbf{X}_m in the reference configuration. Instead of a uniform choice of volume V_m , this partial volume correction $V_m^{(l)}$ is used in Eqs. (39)–(43).

To control the contribution of each Lagrangian point in the peridynamic horizon, the influence function ω is defined by

$$\omega(r) = \begin{cases} C \left(\frac{2}{3} - r^2 + \frac{r^3}{2} \right) & \text{if } r < 1.0, \\ C \frac{(2-r)^3}{6} & \text{if } r \leq 2.0, \\ 0 & \text{otherwise,} \end{cases} \quad (53)$$

in which $r = \frac{2|\xi|}{\epsilon}$ and $C = \frac{15}{7\pi}$ in the two spatial dimensions or $C = \frac{3}{2\pi}$ in the three spatial dimensions. Seleson et al. [57] provide a detailed discussion about the role of influence functions in the peridynamic theory. Note that the modified influence function $\hat{\omega} = \omega I$ is used in our numerical test.

4.1 Non-failure benchmarks

This section presents non-failure benchmarks, including standard benchmark problems in solid mechanics literature, using the IPD method to demonstrate the constitutive correspondence to the classical continuum based theory.

4.1.1 Compression test

We compress a rectangular block to demonstrate a hyperelastic material response under a plain strain. The computational domain is $\Omega = [0, L]^2$, with $L = 40$ cm. A downward uniaxial traction is loaded in the center of the top of the block. Zero horizontal and vertical displacements are respectively applied to the top and bottom boundaries of the block and all other boundaries have zero traction. This test was introduced by Reese et al. [37] to test a stabilization technique for low order finite elements. Fig. 3 provides a schematic of this test case. A shear modulus of $G = 80.194 \frac{\text{dyn}}{\text{cm}^2}$ is used for the incompressible neo-Hookean hyperelastic material, and the downward traction is set to $200 \frac{\text{dyn}}{\text{cm}^2}$. The load time is $T_l = 100$ s, and the final time is $T_f = 500$ s. An additional damping is set to $\eta = 4.0097 \frac{\text{g}}{\text{s}}$. To verify the correspondence to benchmark FE results, material failure (i.e., bond breakage) is not allowed.

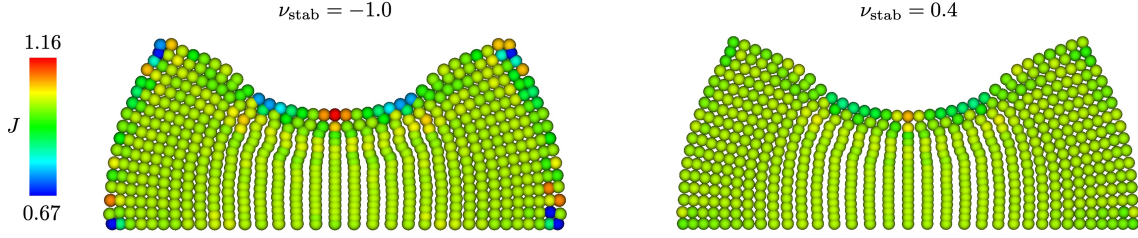


Figure 4: Deformations of the hyperelastic block along with the values of J at material points using the neo-Hookean material model with $G = 80.194 \frac{\text{dyn}}{\text{cm}^2}$. The deformations are computed using 561 solid degrees of freedom (DoF) and $\epsilon = 2.015\Delta X$. The left panel shows the deformation obtained using $\nu_{\text{stab}} = -1.0$, and the right panel shows the result for $\nu_{\text{stab}} = 0.4$.

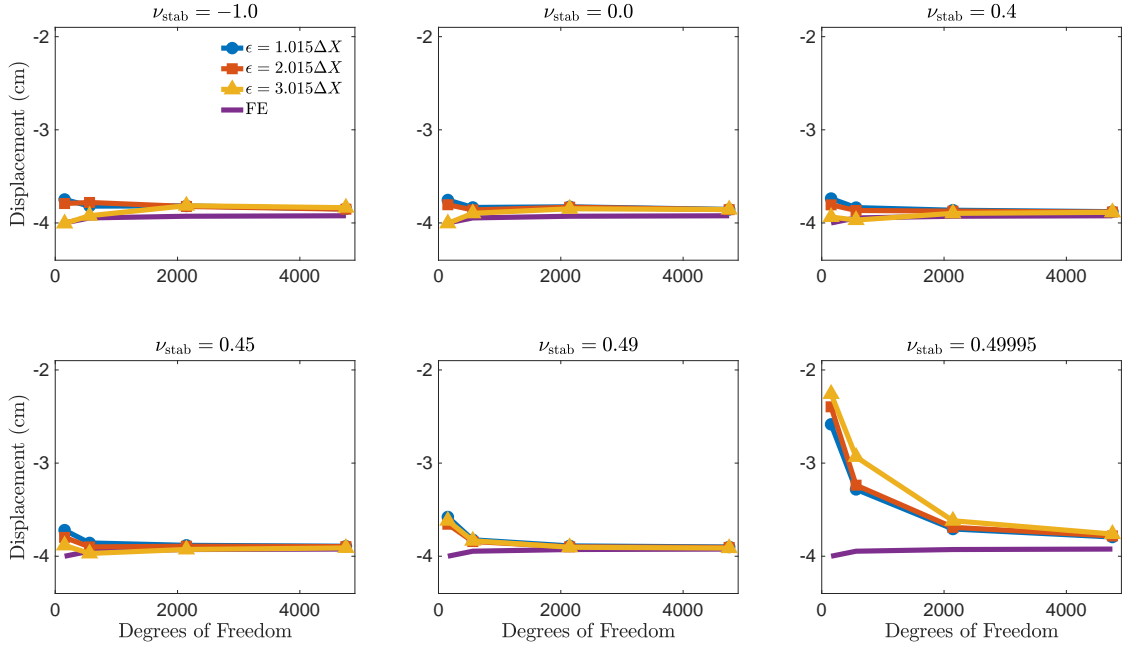


Figure 5: Vertical displacements of the top center point of the compressed block, highlighted in Fig. 3, for different choices of peridynamic horizon size ϵ and numerical Poisson's ratio ν_{stab} . The solid DoF range from 153 to 4753. Note that locking clearly occurs for $\nu_{\text{stab}} = 0.49995$. As in computational standard mechanics approaches, however, the IPD formulation ultimately converges under grid refinement even with high (but fixed) levels of volumetric penalization.

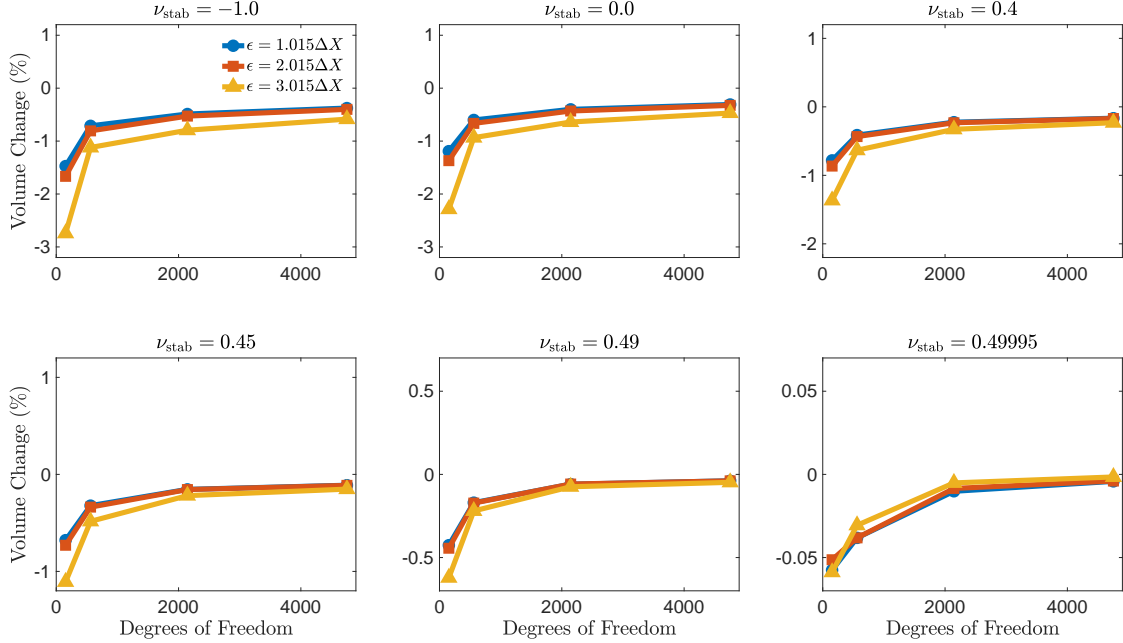


Figure 6: Volume change of the compressed block for different choices of horizon size ϵ and numerical Poisson's ratio ν_{stab} . The solid DoF range from 153 to 4753. The largest change is approximately 2.7%.

Fig. 4 illustrates the material body after the deformation along with pointwise values of the non-local Jacobian determinant J , which is computed using the non-local deformation gradient tensor. Fig. 5 shows the vertical displacements of the top center material point, highlighted in Fig. 3, for various numerical Poisson's ratios ν_{stab} and peridynamic horizon sizes ϵ under grid refinement. The maximum displacement of the point obtained using IPD method is in excellent agreement with that obtained using the standard FE method and it converges under grid refinement to approximately 3.92 cm. The maximum displacement of the point of interest is relatively small (between 2.25 cm and 3.30 cm) at low grid resolutions if a larger value of $\nu_{\text{stab}} = 0.49995$ is used. In the computational mechanics literature, this issue is referred to as volumetric locking and occurs with large volumetric penalties. Note that $\kappa_{\text{stab}} \rightarrow \infty$ as $\nu_{\text{stab}} \rightarrow 0.5$. Under grid refinement, we ultimately recover accurate deformations for fixed finite values of κ_{stab} , as in standard methods for nearly incompressible elasticity.

Fig. 6 shows the volume change observed under deformation for different grid spacings. If ν_{stab} is small, slight volumetric changes occur (between 0.3% and 2.7%) under loading. This volume change becomes negligible (up to 0.001%) when larger values of $\nu_{\text{stab}} \geq 0.4$ are used. This is also clear in Fig. 4. IPD results agree with results obtained using IFED, with both methods exhibiting similar volume changes that range between 0.0004% and 2.1%. Under grid refinement, negligible spurious volume changes or locking occurs in all IPD simulations. In addition, relatively consistent results are obtained for all choices of the PD horizon sizes considered in the tests.

4.1.2 Cook's membrane

Cook's membrane [38], which is a widely used plane-strain problem, is used to demonstrate the hyperelastic material response under bending and shearing. The computational domain is $\Omega = [0, L]^2$, with $L = 40$ cm. Zero displacement is imposed on the left boundary of the structure, and an upward traction of $6.25 \frac{\text{dyn}}{\text{cm}^2}$ is applied to the right boundary. Otherwise, stress-free boundary conditions are assumed. Fig. 7 provides a schematic of this test case. A shear modulus of $G = 83.3333 \frac{\text{dyn}}{\text{cm}^2}$ is used for the incompressible hyperelastic material. The load time is $T_1 = 20$ s, the final time is $T_f = 50$ s, and the damping parameter is set to $\eta = 4.16667 \frac{\text{g}}{\text{s}}$. We focus on the vertical displacements of the top-right corner of the membrane to assess convergence. To impose the same volume fraction at each material point in the NOSB-PD formulation, we

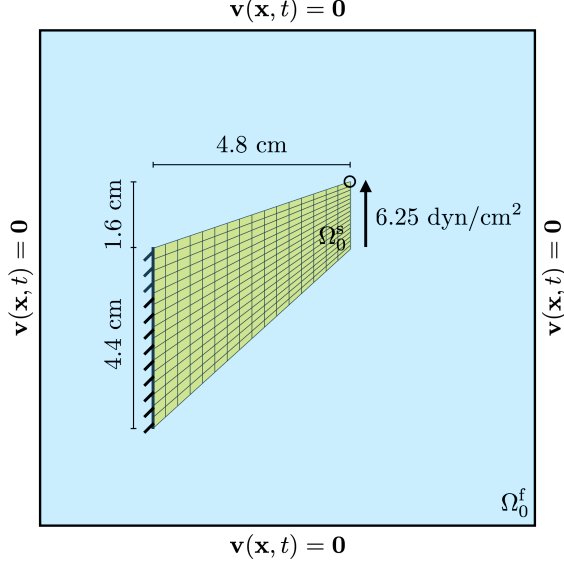


Figure 7: Schematic diagram for the Cook’s membrane benchmark (Sec. 4.1.2). The initial configurations of the immersed structure and a fluid are denoted by Ω_0^s and Ω_0^f , respectively. The entire computational domain is $\Omega = \Omega_0^s \cup \Omega_0^f$. Zero fluid velocity is enforced on the other boundaries of the computational domain.

use a stair-step representation of the immersed membrane. Consequently, a sufficiently large enough horizon size ($\epsilon \geq \sqrt{2}\Delta X$) is required to ensure the sufficient bond connectivity along the material body. Bond breakage is not considered for this problem as well.

Fig. 8 shows the plane sheet after the deformation along with pointwise values of the non-local Jacobian determinant of non-local deformation gradient tensor at each material point. Fig. 9 shows the y -displacement of the top-right corner in Fig. 7 at the steady states for various numerical Poisson’s ratios ν_{stab} and PD horizon sizes ϵ under grid refinement. Fig. 9 shows that the displacements obtained using the IPD method are comparable to those obtained using the classical FE method, and that they converge under grid refinement to approximately 0.67 cm. With $\nu_{\text{stab}} = 0.49995$, a larger volumetric penalty causes volumetric locking, which results in smaller displacements when low mesh resolutions are used in the simulations. However, under grid refinement, we ultimately recover accurate deformations for fixed finite values of numerical bulk modulus, as in classical methods for nearly incompressible elasticity.

Fig. 10 shows volume changes observed under deformation for different grid spacings. With smaller values of ν_{stab} , slight volume changes (between 0.6% and 5.3%) are observed under loading. The volume change becomes negligible (up to 0.0005%) when larger values of $\nu_{\text{stab}} \geq 0.4$ are used. The volume change using IPD is comparable to the results obtained using IFED, which is between 0.000021% and 0.1%. We can expect negligible volume leaking or locking under grid refinement in all IPD simulations. In addition, relatively consistent results are obtained for all considered choices of the PD horizon size.

4.1.3 Torsion

We use a three-dimensional beam under torsion to investigate three dimensional hyperelastic material responses. This benchmark is based on a test suggested by Bonet et al. [58] and later modified by Vadala-Roth et al. [40] to use within the IFED method. The computational domain is the cube $\Omega = [0, L]^3$, with $L = 9$ cm. One side of the beam is fixed in place, and a torsion is applied to the opposite end through displacement boundary conditions. Fig. 11 illustrates the schematic of the test case. The right surface is rotated by the linear function $\theta(t)$ from 0 to $\theta_{T_f} = 2.5\pi$ in time. The maximum angle of rotation is achieved at $T_1 = 0.4T_f$, with $T_f = 5$ s. All other surfaces have zero traction boundary conditions. Material damage and failure are not allowed.

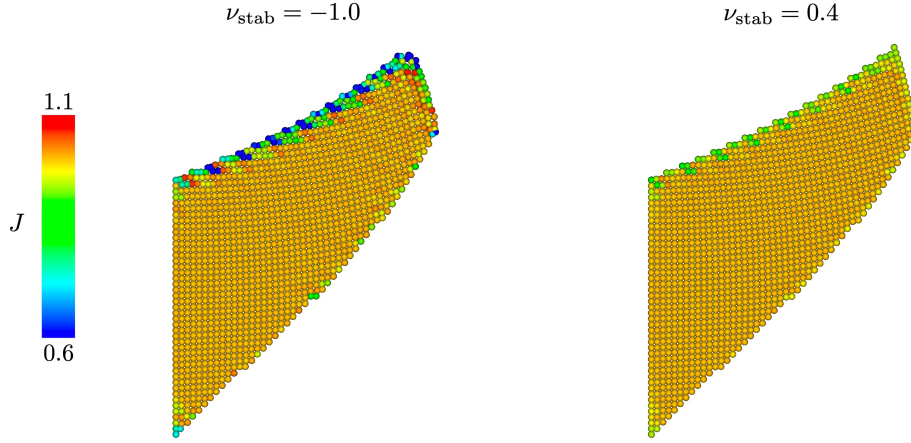


Figure 8: Deformations of Cook's membrane with the values of J at material points using the neo-Hookean material model with $G = 83.3333 \frac{\text{dyn}}{\text{cm}^2}$. The deformations are represented using 1481 solid DoF and $\epsilon = 2.015\Delta X$. The left panel shows the deformation obtained using $\nu_{\text{stab}} = -1.0$, and the right panel shows the result for $\nu_{\text{stab}} = 0.4$.

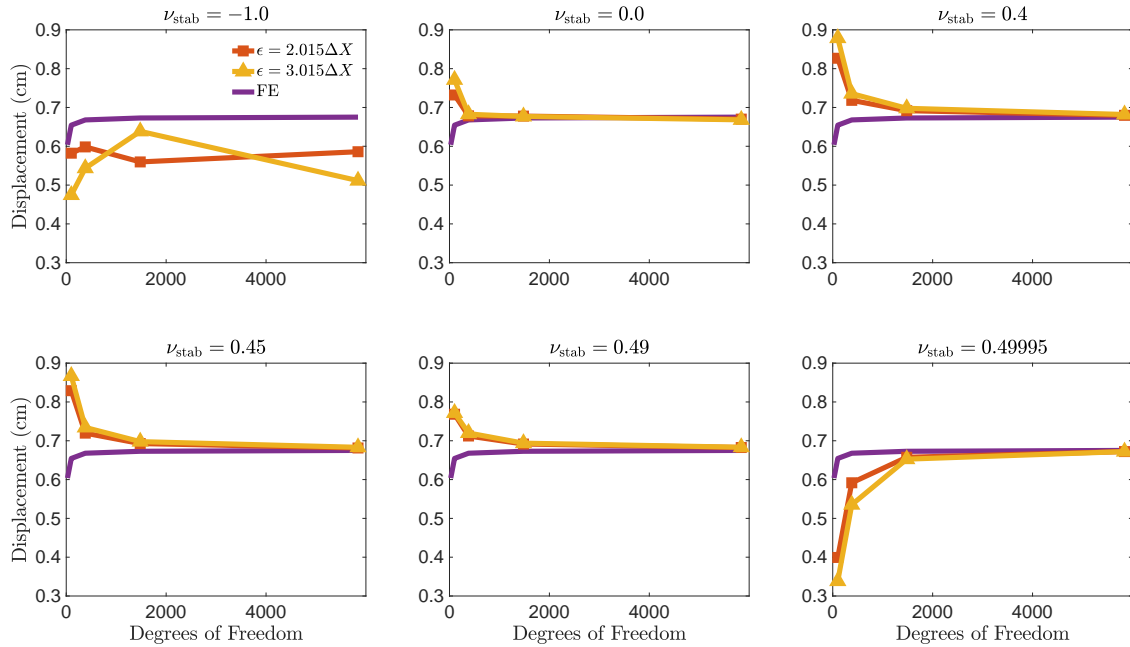


Figure 9: Vertical displacements of the top corner point of the Cook's membrane benchmark, highlighted in Fig. 7, for different choices of peridynamic horizon size ϵ and numerical Poisson's ratio ν_{stab} . The solid DoF range from 101 to 5841. Note that locking clearly occurs for $\nu_{\text{stab}} = 0.49995$. As in standard mechanics approaches, however, the IPD formulation ultimately converges under grid refinement even with high (but fixed) levels of volumetric penalization.

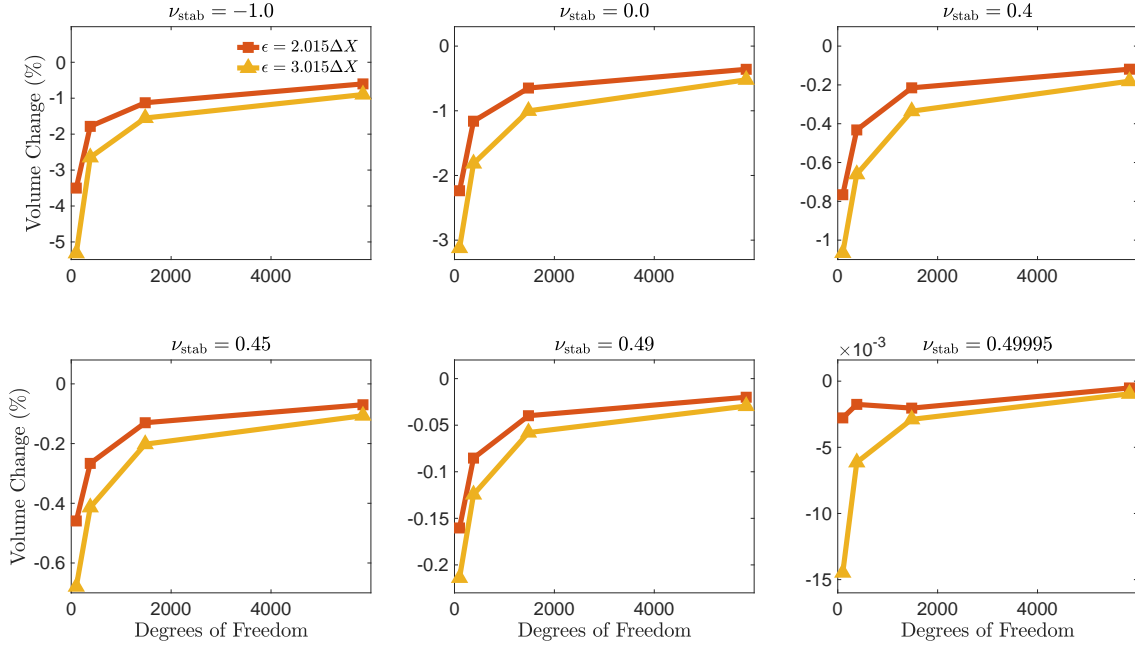


Figure 10: Volume change of the Cook’s membrane benchmark for different choice of horizon size ϵ and numerical Poisson’s ratio ν_{stab} . The solid DoF range from 101 to 5841. The largest change is approximately 5.3%.

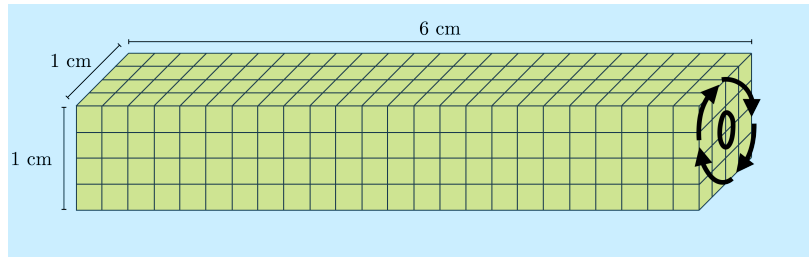


Figure 11: Schematic diagram for the three-dimensional torsion benchmark (Sec. 4.1.3). The computational domain is $\Omega = [0, L]^3$, with $L = 9$ cm, and the three-dimensional beam is placed at the center of the domain. Zero fluid velocity is enforced on the outer boundaries of the computational domain.

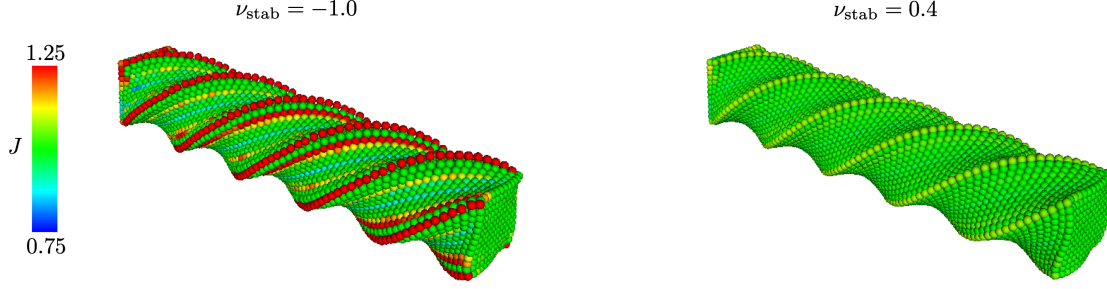


Figure 12: Deformation of the three-dimensional beam with the values of J at material points using the Mooney-Rivlin material model with $c_1 = c_2 = 9000 \frac{\text{dyn}}{\text{cm}^2}$. The deformations are computed using 12337 solid DoF and $\epsilon = 2.015\Delta X$. The left panel shows the deformation obtained using $\nu_{\text{stab}} = -1.0$, and the right panel shows the result for $\nu_{\text{stab}} = 0.4$.

We use the modified Mooney-Rivlin material model [40]

$$\Psi = c_1 \left(J^{-2/3} I_1 - 3 \right) + c_2 \left(\frac{J^{-4/3}}{2} I_2 - 3 \right) + \frac{\kappa_{\text{stab}}}{2} (\ln J)^2, \quad (54)$$

$$\mathbb{P} = 2c_1 J^{-2/3} \left(\mathbb{F} - \frac{I_1}{3} \mathbb{F}^{-T} \right) + 2c_2 J^{-4/3} \left(I_1 \mathbb{F} - \mathbb{F} \mathbb{C} - \frac{I_2}{3} \mathbb{F}^{-T} \right) + \kappa_{\text{stab}} \ln(J) \mathbb{F}^{-T}, \quad (55)$$

in which c_1 and c_2 are material parameters, $I_1 = \text{tr}(\mathbb{C})$, and $I_2 = \text{tr}(\mathbb{C})^2 - \text{tr}(\mathbb{C}^2)$. The material parameters are set to $c_1 = c_2 = 9000 \frac{\text{dyn}}{\text{cm}^2}$, and $G = (c_1 + c_2)$ is used to determine the numerical bulk modulus. The density and viscosity of the surrounding fluid are set to $\rho = 1.0 \frac{\text{g}}{\text{cm}^3}$ and $\mu = 0.04 \frac{\text{dyn}\cdot\text{s}}{\text{cm}^2}$, respectively. This larger value of viscosity compared to the previous benchmarks is used to accelerate reaching the steady state.

Overall deformations and volume conservation using the numerical Poisson's ratio of $\nu_{\text{stab}} = 0.4$ in Sec. 4.1.1 and Sec. 4.1.2 are consistent with the classical elasticity results under grid refinement. In general, a larger value of numerical bulk modulus requires a smaller time step size. For the remainder of the IPD simulations presented herein, we only consider two fixed numerical Poisson's ratios; $\nu_{\text{stab}} = 0.4$ for nearly incompressible hyperelastic material models and $\nu_{\text{stab}} = -1.0$ for comparison tests.

Fig. 12 illustrates the deformations of the beam under torsion along with the Jacobian determinant of the non-local deformation gradient tensor at each material point. Fig. 13a shows the maximum displacement of the center of the top surface in Fig. 11 at the steady states for various sizes of ϵ under grid refinement. The displacements using IPD are comparable to the classical FE results and converge under grid refinement to a value of approximately 0.27 cm. Fig. 13b shows the volume change of the beam for different numbers of the solid DoF, ranging from 0.13% to 7.41%. Volume changes obtained using the IFED method are between 0.16% and 11%, which are comparable to the IPD simulations.

4.1.4 Elastic band

This benchmark examines deformations of an elastic band that are driven by fluid forces themselves. The deformations of the elastic band are simulated under fluid pressure loading. The computational domain is $\Omega = [0, 2L] \times [0, L]$, with $L = 1$ cm. Fluid traction boundary conditions are imposed on the boundaries of the computational domain as $\boldsymbol{\sigma}^f(\mathbf{x}, t)\mathbf{n}(\mathbf{x}) = \mathbf{h}(t) \frac{\text{dyn}}{\text{cm}^2}$ and $\boldsymbol{\sigma}^f(\mathbf{x}, t)\mathbf{n}(\mathbf{x}) = -\mathbf{h}(t) \frac{\text{dyn}}{\text{cm}^2}$ on the left and right, respectively, in which $\mathbf{h}(t) = \left(10 \sin\left(\frac{\pi t}{2T_1}\right), 0 \right)$ when $t < T_1$ and $\mathbf{h}(t) = (10, 0)$ otherwise. The load time is $T_1 = 5$ s. Zero fluid velocity conditions are applied to the top and bottom boundaries of the computational domain. Different from the previous benchmarks, the difference in pressure across the computational domain causes the deformations of the elastic band. Both top and bottom surfaces of the elastic band are attached

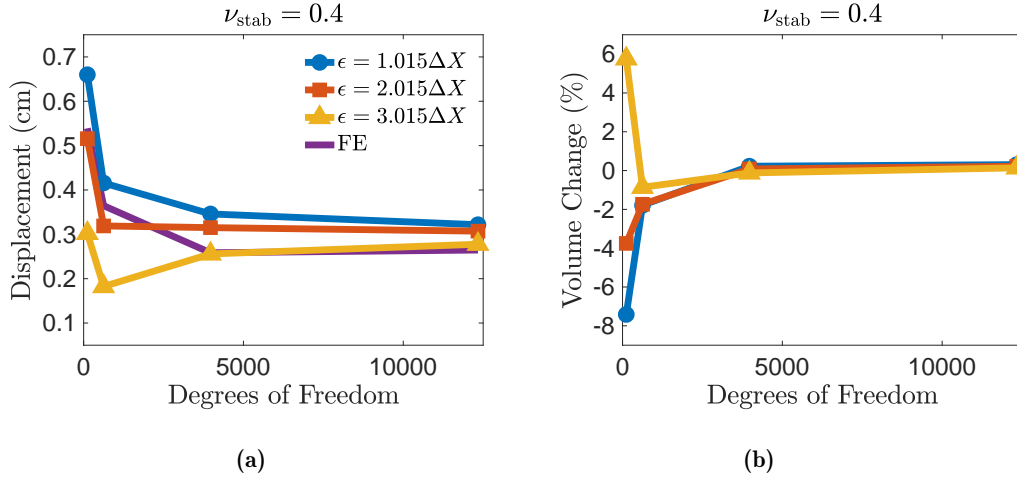


Figure 13: (a) Displacements of the point of interest, highlighted in Fig. 11, for different choices of horizon size ϵ . The solid DoF range from 117 to 12337. (b) Volume change of the beam for different choices of horizon size ϵ .

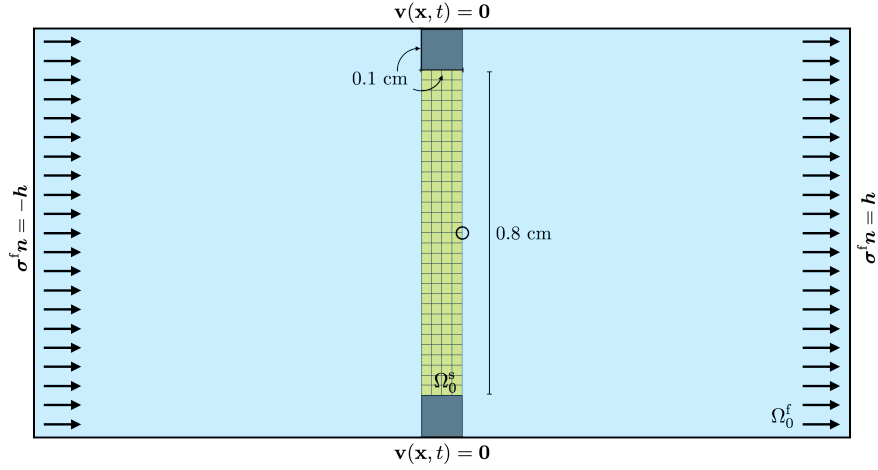


Figure 14: Schematic diagram for the elastic band benchmark (Sec. 4.1.4). The initial configurations of the immersed structure and a fluid are denoted by Ω_0^s and Ω_0^f , respectively. The entire computational domain is $\Omega = \Omega_0^s \cup \Omega_0^f$. Zero fluid velocity is enforced on the top and bottom boundaries of the computational domain, and fluid traction boundary conditions are applied to the left and right boundaries. Fluid traction is set to $\mathbf{h}(t) = \left(10 \sin\left(\frac{\pi t}{2T_1}\right), 0\right) \frac{\text{dyn}}{\text{cm}^2}$ when $t < T_1$ and $\mathbf{h}(t) = (10, 0) \frac{\text{dyn}}{\text{cm}^2}$ otherwise.

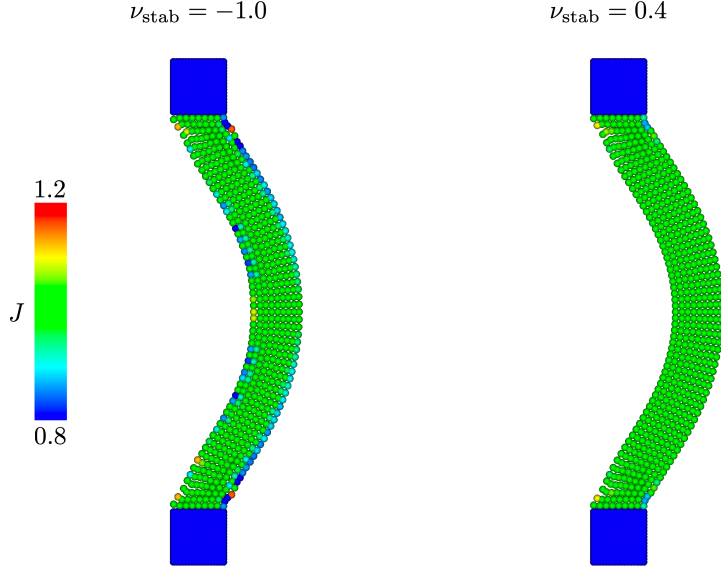


Figure 15: Deformations of an elastic band with the values of J at material points using the neo-Hookean material model with $G = 200 \frac{\text{dyn}}{\text{cm}^2}$. The deformations are computed using 1261 solid degrees of freedom and $\epsilon = 2.015\Delta X$. Note that the number of solid DoF only considers the number of Lagrangian points of the band. The left panel shows the deformation obtained using $\nu_{\text{stab}} = -1.0$, and the right panel shows the result for $\nu_{\text{stab}} = 0.4$.

to rigid blocks. For the sake of computational efficiency, material points in the rigid blocks are not connected to each other; the stationary particles only serve to block the fluid flow between the wall and the flexible band. Fig. 14 provides a schematic of this test case. We measure the maximum displacement of the point of interest, the encircled point in Fig. 14, at $T_f = 15$ s. A shear modulus of $G = 200 \frac{\text{dyn}}{\text{cm}^2}$ is used for the nearly incompressible neo-Hookean material model. Damage and failure of the elastic band are not allowed. An additional damping force in the structure is used with $\eta = 10 \frac{\text{g}}{\text{s}}$, to accelerate reaching steady state.

Fig. 15 shows the deformations of the elastic band under pressure loading at steady state. Fig. 16a shows the maximum horizontal displacement of the point of interest in Fig. 14 at the steady states for different choices of the PD horizon sizes under grid refinement, which is approximately 0.17 cm. Except for $\epsilon = 1.015\Delta X$, the results obtained using the IPD method are comparable to FE results. The absence of a diagonal connectivity in the immersed structure with $\epsilon = 1.015\Delta X$ causes a lack of resistance to this type of bending. Fig. 16b shows volume change of the band for different numbers of the solid DoF. We observe slight volume changes with smaller values of solid DoF, however, these are resolved under grid refinement. The volume conservation achieved by the IPD method (between 0.015% and 1.2%) is comparable to the results generated by the IFED method (between 0.0015% and 2.1%).

To investigate nontrivial fluid dynamics in this benchmark, we test the transient behavior of a dynamic version of the elastic band. Instead of gradually applying the fluid traction as the static problem, fluid traction conditions on the boundaries of the computational domain are set to $\sigma^f(\mathbf{x}, t)\mathbf{n}(\mathbf{x}) = \mathbf{h}(t) \frac{\text{dyn}}{\text{cm}^2}$, in which $\mathbf{h}(t) = (-10, 0)$ and $\mathbf{h}(t) = (10, 0)$ on the left and right, respectively. The final simulation time is set to $T_f = 10$ s. Otherwise, we fix the rest of the test parameters as in the static problem, with no damping.

Fig. 17 shows the structural deformations of the band along with the Eulerian velocity field and the values of Jacobian of the non-local deformation tensor. Fig. 18 shows the transient behavior of the elastic band against time for various numerical Poisson's ratios ν_{stab} and peridynamic horizon sizes ϵ under grid refinement. Fig. 19 shows volume change of the band under deformation for different choices of ν_{stab} and ϵ . The total volume change decreases under grid refinement as in the static case, and the range is comparable to the static case as well. With a larger value of the numerical bulk modulus, the volume change noticeably decreases. Fig. 20a and Fig. 20b show that the maximum displacements of the oscillations and time to

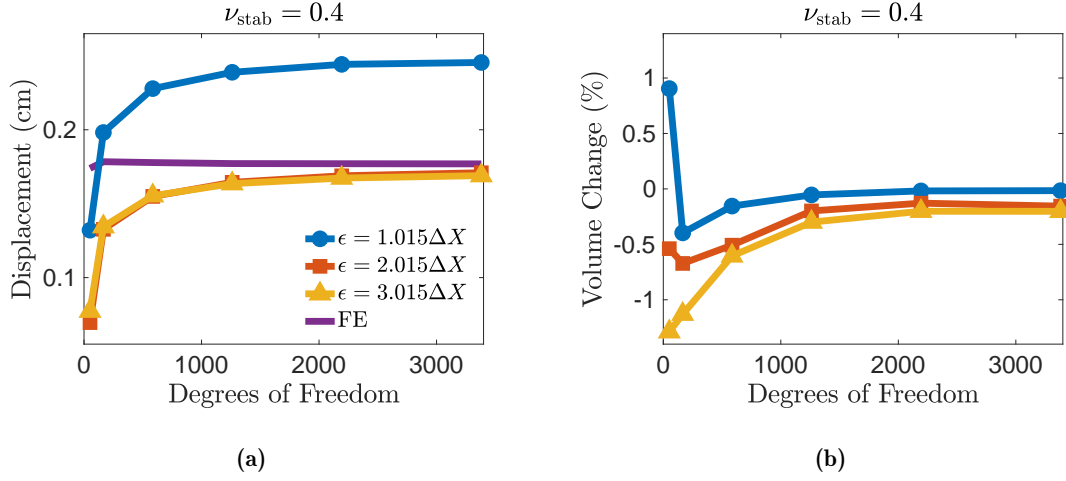


Figure 16: (a) Horizontal displacements of the point of interest, highlighted in Fig. 14, for different choices of horizon size ϵ . The solid DoF range from 51 to 3381. (b) Volume change of the band for different choices of horizon size ϵ .

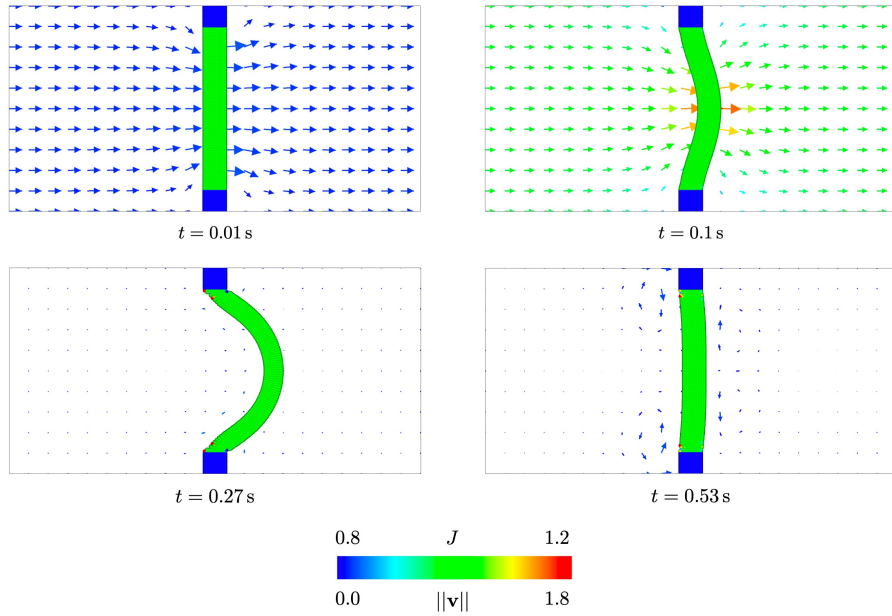


Figure 17: Deformations of a dynamic version of the elastic band under the fluid traction force. The color represents the magnitude of the Eulerian velocity at each spatial point and the values of J at material points. Observe that the Jacobians of the rigid blocks are 0. The deformations are computed using 1261 solid DoF, $\epsilon = 2.015\Delta X$, and $\nu_{\text{stab}} = 0.4$. The band undergoes its largest deformation at $t = 0.27$ s and enters another period of oscillation at $t = 0.53$ s.

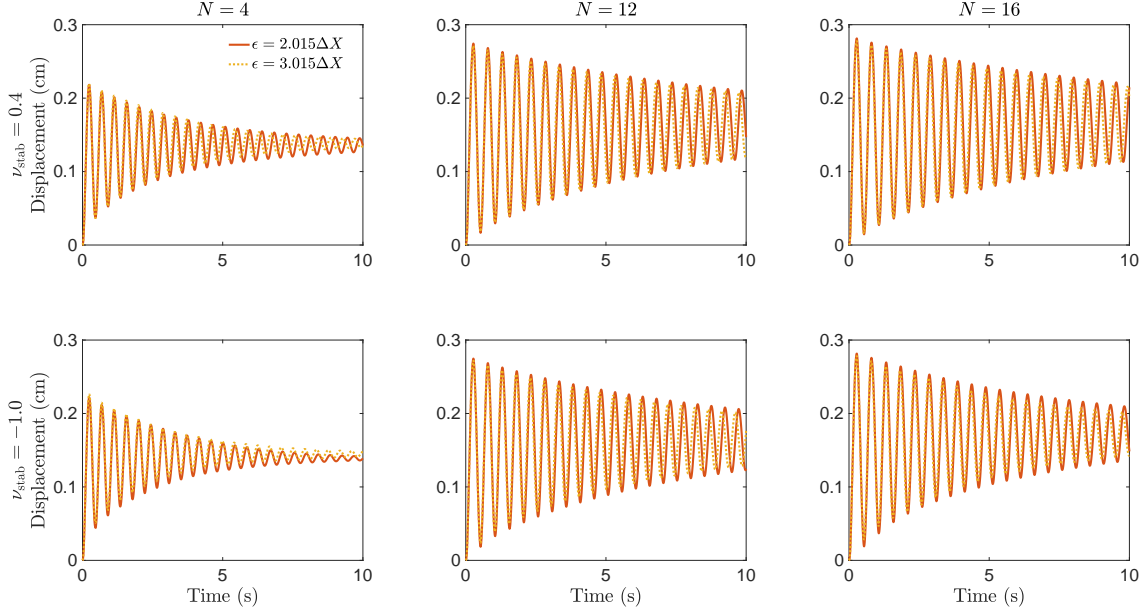


Figure 18: Horizontal displacements of the point of interest, highlighted in Fig. 14, for different choices of horizon size ϵ and numerical Poisson's ratio ν_{stab} under grid refinement. $N = 4$ corresponds to 165 solid DoF, $N = 12$ corresponds to 1261 solid DoF, and $N = 16$ corresponds to 2193 solid DoF.

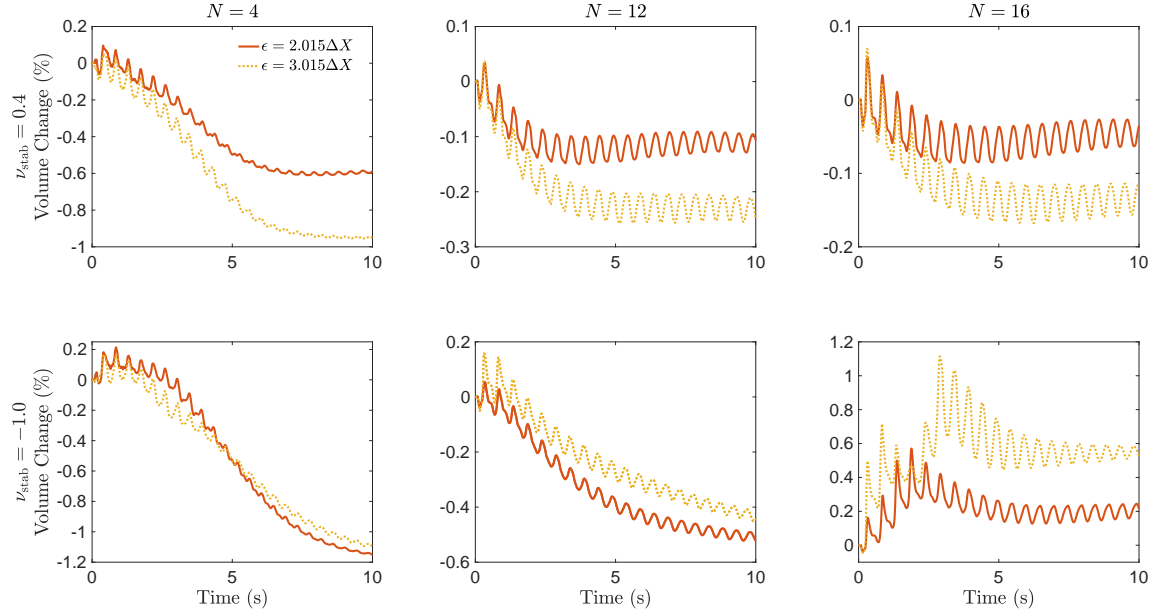


Figure 19: Volume change of the band in Fig. 14 for different choices of horizon size ϵ and numerical Poisson's ratio ν_{stab} under grid refinement. $N = 4$ corresponds to 165 solid DoF, $N = 12$ corresponds to 1261 solid DoF, and $N = 16$ corresponds to 2193 solid DoF.

reach the maximum displacements converge under grid refinement. Fig. 21 shows the upper envelopes of the oscillations for different choices of ϵ under grid refinement.

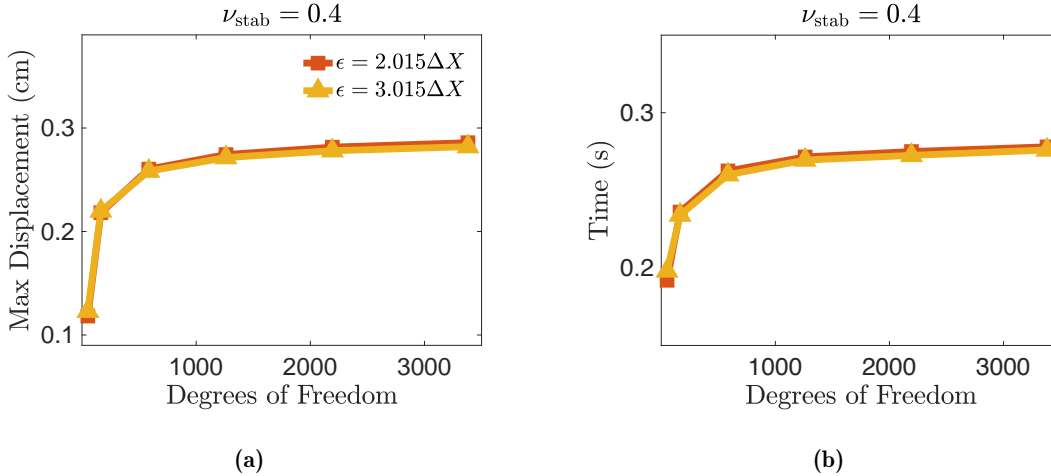


Figure 20: (a) Maximum displacements of the dynamic version of the elastic band for different choices of horizon size ϵ under grid refinement. The solid DoF range from 51 to 3381. (b) Time to reach the maximum displacement of the dynamic version of the elastic band for different choices of horizon size ϵ under grid refinement.

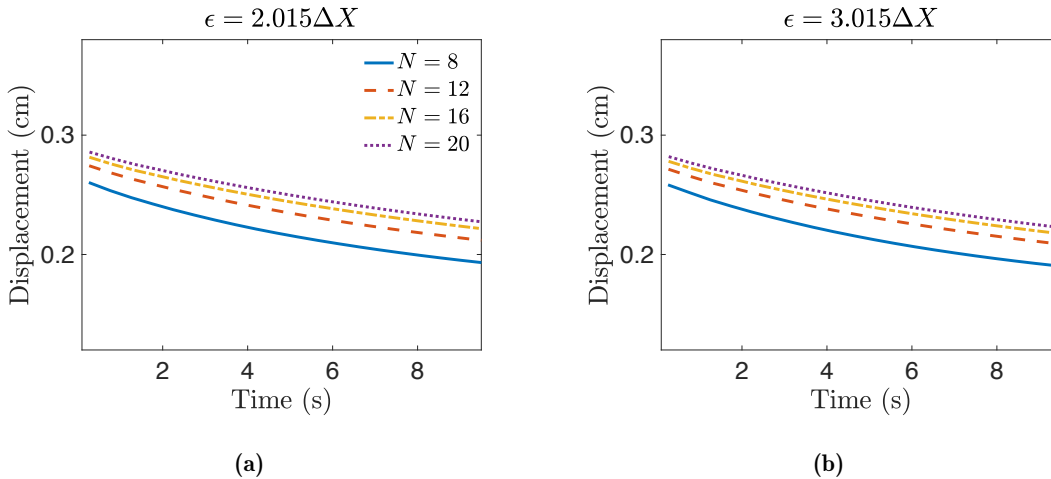


Figure 21: Upper envelopes of the oscillations in Fig. 18 for different choices of horizon size ϵ under grid refinement with $\nu_{\text{stab}} = 0.4$. The solid DoF range from 585 to 3381. $N = 8$ corresponds to 585 solid DoF, $N = 12$ corresponds to 1261 solid DoF, $N = 16$ corresponds to 2193 solid DoF, and $N = 20$ corresponds to 3381.

4.2 Failure benchmarks

This section presents modified elastic band benchmark problems that allow bond breakage to simulate the fluid-driven deformations of a material that can experience damage and, ultimately, failure.

4.2.1 Rupture of an elastic band

This benchmark considers dynamic material deformations and fracture of the elastic band under fluid-driven forces. In this benchmark, the critical bond stretch is set to $s_c = 4.5$ to demonstrate the effectiveness of simulating crack initiation and propagation using the IPD method. In general, the critical bond stretch of a material must be experimentally determined. The critical bond stretch s_c used here is determined based on preliminary tests. The pressure loading is three times larger than the value used in Sec. 4.1.4 on each side;

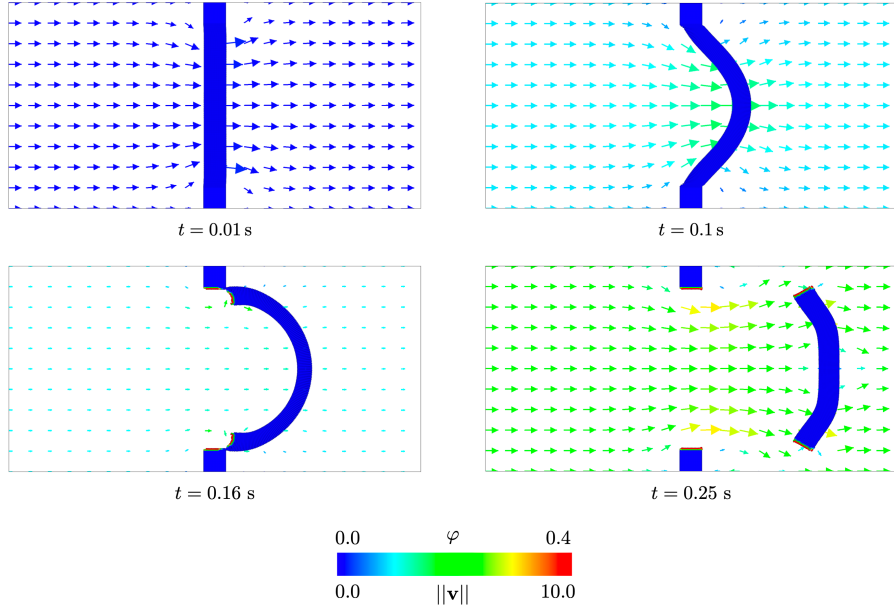


Figure 22: Dynamic failure process of the elastic band with the local damage in NOSB-PD along with the corresponding Eulerian velocity field. Note that $\varphi = 0$ implies that all initial bonds are connected and $\varphi = 1$ implies that all initial bonds are disconnected. The deformations are computed using 3381 solid DoF, $\epsilon = 3.015\Delta X$, and $\nu_{\text{stab}} = 0.4$.

$\boldsymbol{\sigma}^f(\mathbf{x}, t)\mathbf{n}(\mathbf{x}) = \mathbf{h}(t) \frac{\text{dyn}}{\text{cm}^2}$, in which $\mathbf{h}(t) = (-30, 0)$ and $\mathbf{h}(t) = (30, 0)$ on the left and right, respectively. The final simulation time is set to $T_f = 0.25$ s. Otherwise, we use the same parameters as the non-failure case of the dynamic elastic band benchmark. The horizon size is set to $\epsilon = 3.015\Delta X$, as suggested in the PD literature [48].

Fig. 22 shows the crack nucleation and propagation of the dynamic version of the elastic band benchmark with an Eulerian velocity field. The crack formulation is initiated near the junctions between the rigid blocks and the band, and the band gets entirely detached from the block when the bonds exceed the critical bond stretch s_c . Fig. 23a shows the horizontal displacements of the point of interest, highlighted in Fig. 14, for different grid spacings. Fig. 23b shows the local damage growth at the top left corner of the detached band during the failure process under grid refinement.

4.2.2 Elastic band with a notch

We next consider the dynamics of an elastic band with a pre-existing crack. A notch is placed on the center-right of the band with the length of 0.05 cm. The pressure loading is set to $\boldsymbol{\sigma}^f(\mathbf{x}, t)\mathbf{n}(\mathbf{x}) = \mathbf{h}(t) \frac{\text{dyn}}{\text{cm}^2}$, in which $\mathbf{h}(t) = (-20, 0)$ and $\mathbf{h}(t) = (20, 0)$ on the left and right, respectively, with a zero loading time. In this benchmark, the critical bond stretch is set to $s_c = 4.5$ based on preliminary tests. Otherwise, we use the same parameters as the non-failure case of the dynamic elastic band benchmark. To obtain symmetric fracture in the middle of the band, we use even numbers of Lagrangian points in the vertical direction of the elastic band. Fig. 24 provides a schematic of this test case. The horizon size is set to $\epsilon = 3.015\Delta X$, as suggested in the PD literature [48]. The final simulation time is set to $T_f = 0.3$ s.

Fig. 25 shows the dynamic deformation and failure process of the elastic band along with the damage parameter φ and Eulerian velocity vectors. The band undergoes a large deformation before the crack propagates, and it ultimately breaks the bond connectivity and completely ruptures. Fig. 26a shows the vertical displacements of the point A in Fig. 25 under grid refinement, and Fig. 26b shows horizontal displacements of the point A under grid refinement. Fig. 27 shows the local damage growth at the point of interest B

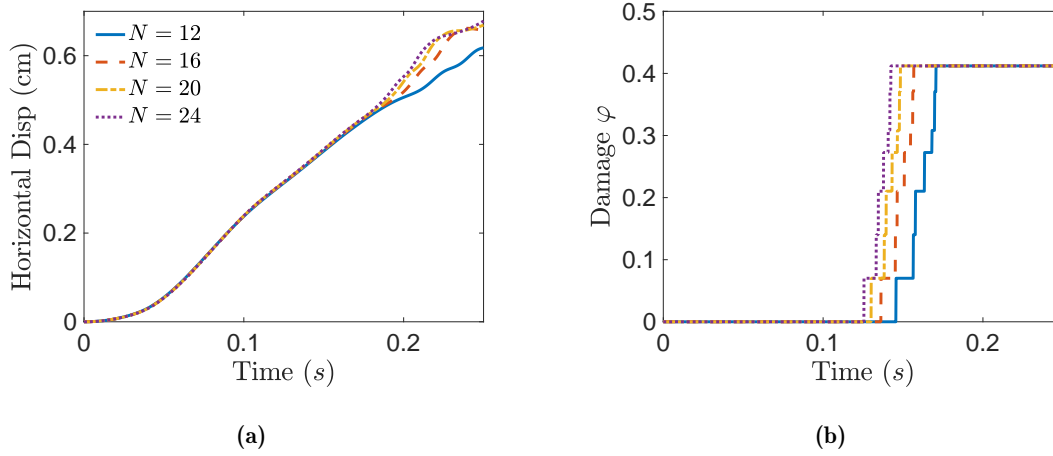


Figure 23: (a): Horizontal displacements of the point of interest, highlighted in Fig. 14, under grid refinement. (b): Local damage growth at the top left corner of the detached band during the failure process under grid refinement. $N = 12$ corresponds to 1261 solid DoF, $N = 16$ corresponds to 2193 solid DoF, $N = 20$ corresponds to 3381, and $N = 24$ corresponds to 4825.

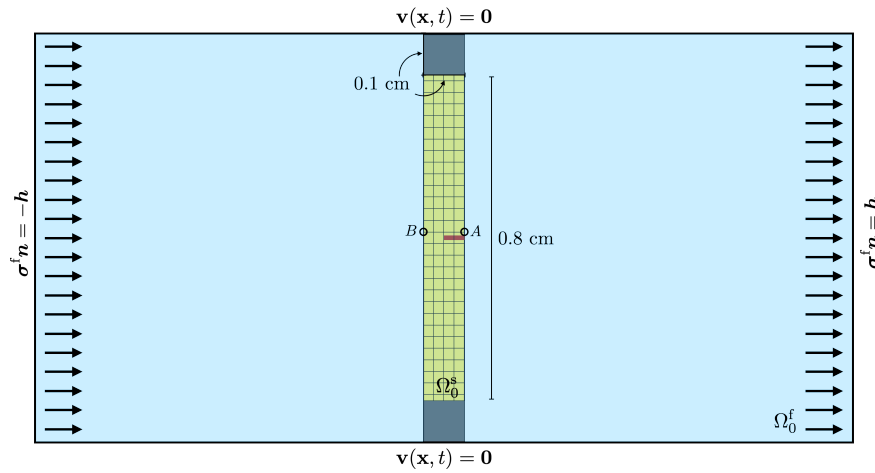


Figure 24: Schematic diagram for the failed elastic band benchmark (Sec. 4.2.2). The initial configurations of the immersed structure and a fluid are denoted by Ω_0^s and Ω_0^f , respectively. The entire computational domain is $\Omega = \Omega_0^s \cup \Omega_0^f$. Zero fluid velocity is enforced on the top and bottom boundaries of the computational domain, and fluid traction boundary conditions are applied to the left and right boundaries. Fluid traction is set to $\mathbf{h}(t) = (20, 0) \frac{\text{dyn}}{\text{cm}^2}$.

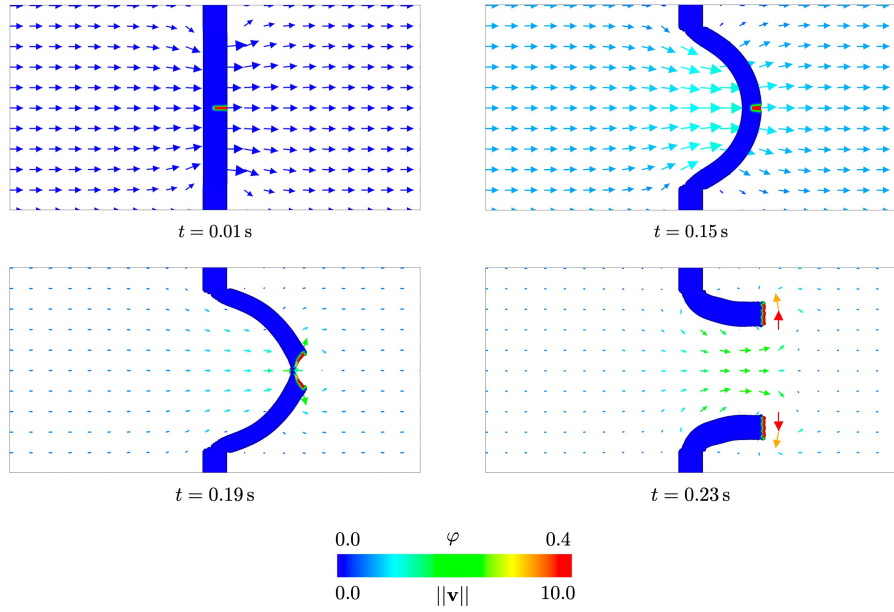


Figure 25: Dynamic failure process of the elastic band with the local damage in NOSB-PD along with the corresponding Eulerian velocity field. Note that $\varphi = 1$ indicates all initially connected bonds are broken. The deformations are computed using 2210 solid DoF, $\epsilon = 3.015\Delta X$, and $\nu_{\text{stab}} = 0.4$.

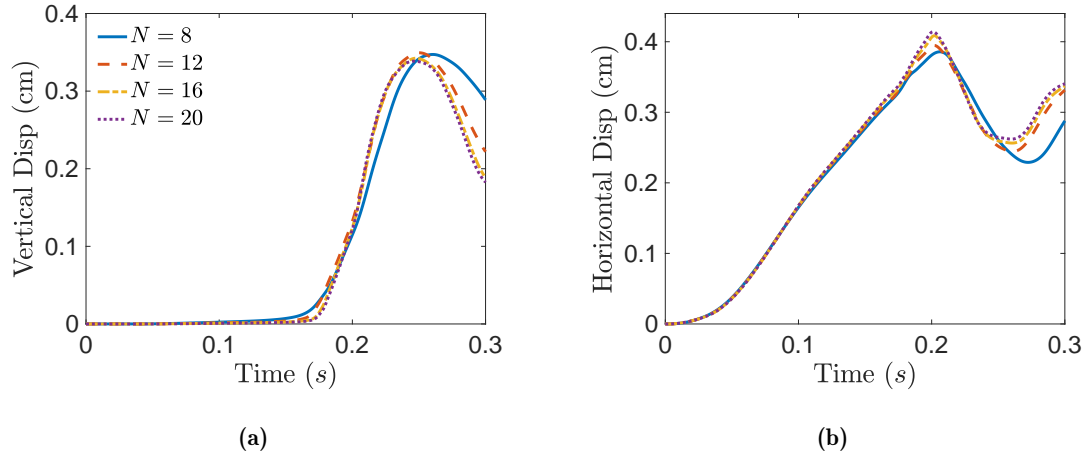


Figure 26: (a): Vertical displacements of the point of interest A, highlighted in Fig. 25, under grid refinement. (b): Horizontal displacements of the point of interest A under grid refinement. $N = 8$ corresponds to 594 solid DoF, $N = 12$ corresponds to 1274 solid DoF, $N = 16$ corresponds to 2210 solid DoF, and $N = 20$ corresponds to 3402.

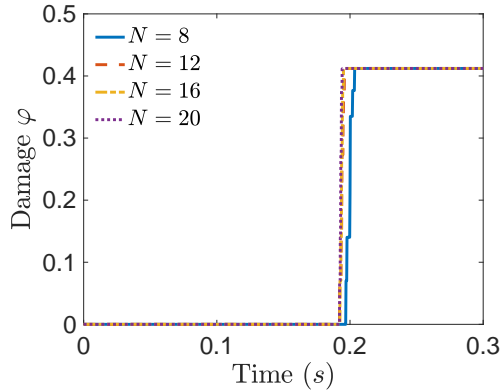


Figure 27: Local damage growth at the point of interest B, highlighted in Fig. 25, during the failure process. $N = 8$ corresponds to 594 solid DoF, $N = 12$ corresponds to 1274 solid DoF, $N = 16$ corresponds to 2210 solid DoF, and $N = 20$ corresponds to 3402. Note that $\varphi = 0$ implies that all initial bonds are connected and $\varphi = 1$ implies that all initial bonds are disconnected.

during the failure process under grid refinement.

5 Discussion and conclusion

This paper develops an immersed peridynamics method to simulate FSI with material models that can experience material damage and failure. It uses non-ordinary state-based peridynamics to determine the internal body forces, which allows nonlinear material models of the immersed structural body that can accommodate discontinuities (i.e., crack formulation and propagation). Numerical tests consider both classical quasi-static benchmarks adapted from the solid mechanics literature [37–39] and fully dynamic FSI benchmarks [40]. Our numerical results demonstrate the constitutive correspondence of nonlinear hyperelastic material models for non-failure benchmarks, as detailed in Sec. 4.1, and show that the IPD method yields comparable accuracy under grid refinement that offered by a stabilized FE method [37] and the IFED method [40]. We obtain accurate results of overall deformations and volume conservation. We also test crack initiation, growth, and fracture in the immersed structural body by fluid stresses, as detailed in Sec. 4.2, and simulation results show ϵ -convergence as in the non-failure benchmarks. Moreover, we investigate the effect of the size of the peridynamic horizon using standard solid mechanics and FSI benchmark studies. When the IPD method is used with classical solid mechanics benchmarks, results are relatively insensitive to the size of the peridynamic horizons. In contrast, the elastic band benchmarks requires at least $\epsilon = 2.015\Delta X$ for non-failure tests and $\epsilon = 3.015\Delta X$ for failure tests.

An interesting finding of this work is that the IPD method with a proper volume stabilization does not appear to suffer from zero-energy (hourglass) mode. In general, zero-energy modes (or hourglass instabilities) in deformed material bodies caused by the non-local deformation gradient tensor are observed in numerical implementations of the peridynamic correspondence model. Several numerical treatments have been developed to reduce such instabilities [59–62]. The methodology developed herein appears to avoid the need to use such techniques, which eliminates substantial numerical parameter tuning.

Our current IPD formulation is limited to a material that has uniformly distributed volumes along the structural body, which limits the fidelity of the methodology for complex structural geometries. This can be seen in the Cook’s membrane benchmark Sec. 4.1.2 with the stair-step geometry. To simulate the deformations of real hyperelastic materials under fluid traction, it is necessary to modify the volume terms in the discrete IPD formulation Eqs. (39)–(43). Such modifications will ultimately enable the IPD method to simulate realistic material behaviors in more complex FSI problems. We also only consider isotropic material models. An important extension of this work will be to consider anisotropic, fiber-reinforced material models like those that have been developed to describe biomaterials.

Acknowledgement

We gratefully acknowledge research support through NIH Award HL 117063 and NSF Awards OAC 1450327, OAC 1652541, OAC 1931516, and DMS 1929298. A.P.S.B acknowledges support through NSF Award OAC 1931368. We thank Jae H. Lee, Simone Rossi, and Pablo Selson for their constructive feedback in improving the manuscript. Numerical simulations were performed using facilities provided by the University of North Carolina at Chapel Hill through the Research Computing division of UNC Information Technology Services.

References

- [1] A. A. Griffith, The phenomena of rupture and flow in solids, *Philosophical Transactions of the Royal Society of London. Series A* 221 (582-593) (1921) 163–198.
- [2] A. Hillerborg, M. Mod er, P.-E. Petersson, Analysis of crack formation and crack growth in concrete by means of fracture mechanics and finite elements, *Cement and Concrete Research* 6 (6) (1976) 773–781.
- [3] N. Mo s, J. Dolbow, T. Belytschko, A finite element method for crack growth without remeshing, *International Journal for Numerical Methods in Engineering* 46 (1) (1999) 131–150.
- [4] S. A. Silling, Reformulation of elasticity theory for discontinuities and long-range forces, *Journal of the Mechanics and Physics of Solids* 48 (1) (2000) 175–209.
- [5] W. Gerstle, N. Sau, S. Silling, Peridynamic modeling of plain and reinforced concrete structures, 18th *International Conference on Structural Mechanics in Reactor Technology* (2005) 54–68.
- [6] S. A. Silling, M. Epton, O. Weckner, J. Xu, E. Askari, Peridynamic states and constitutive modeling, *Journal of Elasticity* 88 (2) (2007) 151–184.
- [7] T. L. Warren, S. A. Silling, A. Askari, O. Weckner, M. A. Epton, J. Xu, A non-ordinary state-based peridynamic method to model solid material deformation and fracture, *International Journal of Solids and Structures* 46 (5) (2009) 1186–1195.
- [8] C. S. Peskin, The immersed boundary method, *Acta Numerica* 11 (2002) 479–517.
- [9] C. S. Peskin, Flow patterns around heart valves: a numerical method, *Journal of Computational Physics* 10 (2) (1972) 252–271.
- [10] C. S. Peskin, Numerical analysis of blood flow in the heart, *Journal of Computational Physics* 25 (3) (1977) 220–252.
- [11] C. S. Peskin, D. M. McQueen, A three-dimensional computational method for blood flow in the heart i. immersed elastic fibers in a viscous incompressible fluid, *Journal of Computational Physics* 81 (2) (1989) 372–405.
- [12] D. M. McQueen, C. S. Peskin, A three-dimensional computational method for blood flow in the heart. ii. contractile fibers, *Journal of Computational Physics* 82 (2) (1989) 289–297.
- [13] D. M. McQueen, C. S. Peskin, A three-dimensional computer model of the human heart for studying cardiac fluid dynamics, *Computer Graphics* 34 (1) (2000) 56–60.
- [14] D. M. McQueen, C. S. Peskin, Heart simulation by an immersed boundary method with formal second-order accuracy and reduced numerical viscosity, in: *Mechanics for a New Millennium*, Kluwer Academic Publishers, 2002, pp. 429–444.
- [15] B. E. Griffith, X. Luo, D. M. McQueen, C. S. Peskin, Simulating the fluid dynamics of natural and prosthetic heart valves using the immersed boundary method, *International Journal of Applied Mechanics* 01 (01) (2009) 137–177.

- [16] B. E. Griffith, Immersed boundary model of aortic heart valve dynamics with physiological driving and loading conditions, *International Journal for Numerical Methods in Biomedical Engineering* 28 (3) (2012) 317–345.
- [17] J. H. Lee, A. D. Rygg, E. M. Kolahdouz, S. Rossi, S. M. Retta, N. Duraiswamy, L. N. Scotten, B. A. Craven, B. E. Griffith, Fluid–structure interaction models of bioprosthetic heart valve dynamics in an experimental pulse duplicator, *Annals of Biomedical Engineering* 48 (5) (2020) 1475–1490.
- [18] J. H. Lee, L. N. Scotten, R. Hunt, T. G. Caranasos, J. P. Vavalle, B. E. Griffith, Bioprosthetic aortic valve diameter and thickness are directly related to leaflet fluttering: Results from a combined experimental and computational modeling study, *JTCVS Open* 6 (2021) 60–81.
- [19] Y. J. Choi, V. Vedula, R. Mittal, Computational study of the dynamics of a bileaflet mechanical heart valve in the mitral position, *Annals of Biomedical Engineering* 42 (8) (2014) 1668–1680.
- [20] S. Bailoor, J.-H. Seo, L. P. Dasi, S. Schena, R. Mittal, A computational study of the hemodynamics of bioprosthetic aortic valves with reduced leaflet motion, *Journal of Biomechanics* 120 (2021) 110350.
- [21] E. M. Kolahdouz, A. P. S. Bhalla, B. A. Craven, B. E. Griffith, An immersed interface method for discrete surfaces, *Journal of Computational Physics* 400 (2020) 108854.
- [22] W. Kou, A. P. S. Bhalla, B. E. Griffith, J. E. Pandolfino, P. J. Kahrilas, N. A. Patankar, A fully resolved active musculo-mechanical model for esophageal transport, *Journal of Computational Physics* 298 (2015) 446–465.
- [23] W. Kou, B. E. Griffith, J. E. Pandolfino, P. J. Kahrilas, N. A. Patankar, A continuum mechanics-based musculo-mechanical model for esophageal transport, *Journal of Computational Physics* 348 (2017) 433–459.
- [24] A. P. S. Bhalla, B. E. Griffith, N. A. Patankar, A forced damped oscillation framework for undulatory swimming provides new insights into how propulsion arises in active and passive swimming, *PLoS Computational Biology* 9 (6) (2013) e1003097.
- [25] A. P. S. Bhalla, R. Bale, B. E. Griffith, N. A. Patankar, A unified mathematical framework and an adaptive numerical method for fluid–structure interaction with rigid, deforming, and elastic bodies, *Journal of Computational Physics* 250 (2013) 446–476.
- [26] G. Herschlag, L. Miller, Reynolds number limits for jet propulsion: A numerical study of simplified jellyfish, *Journal of Theoretical Biology* 285 (1) (2011) 84–95.
- [27] S. Kern, P. Koumoutsakos, Simulations of optimized anguilliform swimming, *Journal of Experimental Biology* 209 (24) (2006) 4841–4857.
- [28] I. Borazjani, L. Ge, F. Sotiropoulos, Curvilinear immersed boundary method for simulating fluid structure interaction with complex 3d rigid bodies, *Journal of Computational Physics* 227 (16) (2008) 7587–7620.
- [29] I. Borazjani, F. Sotiropoulos, Numerical investigation of the hydrodynamics of carangiform swimming in the transitional and inertial flow regimes, *Journal of Experimental Biology* 211 (10) (2008) 1541–1558.
- [30] A. Santhanakrishnan, S. Jones, W. Dickson, M. Peek, V. Kasoju, M. Dickinson, L. Miller, Flow structure and force generation on flapping wings at low reynolds numbers relevant to the flight of tiny insects, *Fluids* 3 (3) (2018) 45.
- [31] Z. J. Wang, Dissecting insect flight, *Annual Review of Fluid Mechanics* 37 (1) (2005) 183–210.
- [32] B. E. Griffith, N. A. Patankar, Immersed methods for fluid–structure interaction, *Annual Review of Fluid Mechanics* 52 (2020) 421–448.

- [33] B. E. Griffith, X. Luo, Hybrid finite difference/finite element immersed boundary method, *International Journal for Numerical Methods in Biomedical Engineering* 33 (12) (2017) e2888.
- [34] D. Boffi, L. Gastaldi, L. Heltai, C. S. Peskin, On the hyper-elastic formulation of the immersed boundary method, *Computer Methods in Applied Mechanics and Engineering* 197 (25) (2008) 2210–2231.
- [35] L. Zhang, A. Gerstenberger, X. Wang, W. K. Liu, Immersed finite element method, *Computer Methods in Applied Mechanics and Engineering* 193 (21) (2004) 2051–2067.
- [36] D. Wells, B. Vadala-Roth, J. H. Lee, B. E. Griffith, A nodal immersed finite element-finite difference method (2021). [arXiv:2111.09958](https://arxiv.org/abs/2111.09958).
- [37] S. Reese, M. Küssner, B. D. Reddy, A new stabilization technique for finite elements in non-linear elasticity, *International Journal for Numerical Methods in Engineering* 44 (11) (1999) 1617–1652.
- [38] R. D. Cook, Improved two-dimensional finite element, *Journal of the Structural Division* 100 (9) (1974) 1851–1863.
- [39] J. Bonet, R. D. Wood, *Nonlinear Continuum Mechanics for Finite Element Analysis*, Cambridge University Press, Cambridge, 1997.
- [40] B. Vadala-Roth, S. Acharya, N. A. Patankar, S. Rossi, B. E. Griffith, Stabilization approaches for the hyperelastic immersed boundary method for problems of large-deformation incompressible elasticity, *Computer Methods in Applied Mechanics and Engineering* 365 (2020) 112978.
- [41] R. Glowinski, T.-W. Pan, T. Hesla, D. Joseph, A distributed lagrange multiplier/fictitious domain method for particulate flows, *International Journal of Multiphase Flow* 25 (5) (1999) 755–794.
- [42] N. Patankar, P. Singh, D. Joseph, R. Glowinski, T.-W. Pan, A new formulation of the distributed lagrange multiplier/fictitious domain method for particulate flows, *International Journal of Multiphase Flow* 26 (9) (2000) 1509–1524.
- [43] R. Glowinski, T. Pan, T. Hesla, D. Joseph, J. Périaux, A fictitious domain approach to the direct numerical simulation of incompressible viscous flow past moving rigid bodies: Application to particulate flow, *Journal of Computational Physics* 169 (2) (2001) 363–426.
- [44] M. Hillman, M. Pasetto, G. Zhou, Generalized reproducing kernel peridynamics: unification of local and non-local meshfree methods, non-local derivative operations, and an arbitrary-order state-based peridynamic formulation, *Computational Particle Mechanics* 7 (2) (2019) 435–469.
- [45] E. Madenci, E. Oterkus, *Peridynamic Theory and Its Applications*, Springer, New York, 2014.
- [46] S. A. Silling, E. Askari, A meshfree method based on the peridynamic model of solid mechanics, *Computers & Structures* 83 (17-18) (2005) 1526–1535.
- [47] J. T. Foster, S. A. Silling, W. Chen, An energy based failure criterion for use with peridynamic states, *International Journal for Multiscale Computational Engineering* 9 (6) (2011).
- [48] D. Behera, P. Roy, E. Madenci, Peridynamic correspondence model for finite elastic deformation and rupture in neo-hookean materials, *International Journal of Non-Linear Mechanics* 126 (2020) 103564.
- [49] B. E. Griffith, An accurate and efficient method for the incompressible navier–stokes equations using the projection method as a preconditioner, *Journal of Computational Physics* 228 (20) (2009) 7565–7595.
- [50] P. Colella, P. R. Woodward, The piecewise parabolic method (PPM) for gas-dynamical simulations, *Journal of Computational Physics* 54 (1) (1984) 174–201.
- [51] B. E. Griffith, R. D. Hornung, D. M. McQueen, C. S. Peskin, An adaptive, formally second order accurate version of the immersed boundary method, *Journal of Computational Physics* 223 (1) (2007) 10–49.

- [52] IBAMR: An adaptive and distributed-memory parallel implementation of the immersed boundary method, <https://ibamr.github.io/>.
- [53] S. A. Silling, R. B. Lehoucq, Convergence of peridynamics to classical elasticity theory, *Journal of Elasticity* 93 (1) (2008) 13.
- [54] P. Seleson, D. J. Littlewood, Convergence studies in meshfree peridynamic simulations, *Computers & Mathematics with Applications* 71 (11) (2016) 2432–2448.
- [55] W. Hu, Y. Ha, F. Bobaru, Numerical integration in peridynamics, technical report, University of Nebraska-Lincoln, Department of Mechanical and Materials Engineering (2010).
- [56] P. Seleson, D. J. Littlewood, Numerical tools for improved convergence of meshfree peridynamic discretizations, in: *Handbook of Nonlocal Continuum Mechanics for Materials and Structures*, Springer International Publishing, 2017, pp. 1–27.
- [57] P. Seleson, M. Parks, On the role of the influence function in the peridynamic theory, *International Journal for Multiscale Computational Engineering* 9 (6) (2011) 689–706.
- [58] J. Bonet, A. J. Gil, R. Ortigosa, A computational framework for polyconvex large strain elasticity, *Computer Methods in Applied Mechanics and Engineering* 283 (2015) 1061–1094.
- [59] S. A. Silling, Stability of peridynamic correspondence material models and their particle discretizations, *Computer Methods in Applied Mechanics and Engineering* 322 (2017) 42–57.
- [60] X. Gu, Q. Zhang, Y. Yu, An effective way to control numerical instability of a nonordinary state-based peridynamic elastic model, *Mathematical Problems in Engineering* 2017 (2017).
- [61] J. Luo, V. Sundararaghavan, Stress-point method for stabilizing zero-energy modes in non-ordinary state-based peridynamics, *International Journal of Solids and Structures* 150 (2018) 197–207.
- [62] S. R. Chowdhury, P. Roy, D. Roy, J. Reddy, A modified peridynamics correspondence principle: Removal of zero-energy deformation and other implications, *Computer Methods in Applied Mechanics and Engineering* 346 (2019) 530–549.